

Investigating chemical variations between interstellar gas clouds in the Solar neighbourhood

T. Ramburuth-Hurt¹, A. De Cia^{1,2}, J.-K. Krogager^{3,4}, C. Ledoux⁵, E. Jenkins⁶, A. J. Fox^{7,8}, C. Konstantopoulou¹, A. Velichko^{1,9}, and L. Dalla Pola¹

¹ Department of Astronomy, University of Geneva, Chemin Pegasi 51, Versoix, Switzerland

² European Southern Observatory, Karl-Schwarzschild-Str. 2, 85748 Garching, Germany

³ Université Claude Bernard Lyon 1, Centre de Recherche Astrophysique de Lyon UMR5574, 9 Av. Charles André, 69230 Saint-Genis-Laval, France

⁴ French-Chilean Laboratory for Astronomy (FCLA), CNRS-IRL3386, U. de Chile, Camino el Observatorio 1515, Casilla 36-D, Santiago, Chile

⁵ European Southern Observatory, Alonso de Córdova 3107, Vitacura, Casilla 19001, Santiago, Chile

⁶ Department of Astrophysical Sciences, Princeton University, Princeton, NJ 08544-1001, USA

⁷ AURA for ESA, Space Telescope Science Institute, 3700 San Martin Drive, Baltimore, MD 21218, USA

⁸ Department of Physics & Astronomy, Johns Hopkins University, 3400 N. Charles Street, Baltimore, MD 21218, USA

⁹ Institute of Astronomy, Kharkiv National University, 4 Svobody Sq., Kharkiv, 61022, Ukraine

Received xx; accepted yy

ABSTRACT

The interstellar medium (ISM) is a fundamental component of the Milky Way. Studying its chemical composition and the level of its chemical diversity gives us insight into the evolution of the Milky Way and the role of gas in the Galactic environment. In this paper, we use a novel simulation technique to model the distribution of total hydrogen between gas components, and therefore derive new constraints on the dust depletion and metallicity. We study individual gas components along the lines of sight towards eight bright O/B stars within 1.1 kpc of the Sun using high-resolution HST/STIS absorption spectra ($R \sim 114\,000$). We measure the level of dust depletion for these individual components and find components with higher levels of dust depletion compared to Milky Way sightlines in the literature. We find large ranges in the level of dust depletion among components along lines of sight, up to 1.19 dex. Although it is not possible to directly measure the metallicity of individual components due to the saturated and damped Lyman- α line, we investigate possible metallicity ranges for individual gas components by exploring many different distributions of the total hydrogen gas between components. We select possible combinations of these gas fractions which produce the minimum metallicity difference between components, and for these cases we determine individual metallicities to accuracies that range between ~ 0.1 to 0.4 dex. This work shows that full line-of-sight analyses wash out the level of diversity along lines of sight, and that component-by-component studies give a more in-depth understanding of the chemical intricacies of the interstellar medium.

Key words. Milky Way – interstellar medium – absorption-line spectroscopy – metallicity – dust depletion

1. Introduction

Studies of the chemical composition of the Milky Way's interstellar medium (ISM) give us important insight into its evolution and the role of gas in the Galactic environment. Determining the level of diversity in the metallicity of the warm neutral gas in the Solar neighbourhood is important for finding evidence of low-metallicity gas in-fall onto the Milky Way, for example from high-velocity clouds (HVCs, Richter 2017; Fox et al. 2019). Low-metallicity gas inflows from the circumgalactic medium (CGM) have been predicted in simulations (Schaye et al. 2015; Crain et al. 2015; Nelson et al. 2019; Pillepich et al. 2019; Péroux et al. 2020). Evidence for pockets of low-metallicity gas in the ISM of the Milky Way could be an indication of low-metallicity gas in-fall De Cia et al. (2021).

Absorption-line spectroscopy is a powerful method for studying the metal content of the gas in galaxies because it gives access to the column densities of many metals (ions), and the methods of measuring the column densities are very robust. Additionally, UV absorption-line spectroscopy is particularly valuable because the resonant lines of the most dominant ionisation

states of the most abundant cosmic metals (O, C, Fe, Si, etc.) are available in the UV. There are several phenomena to take into account when calculating the total overall metallicity (i.e. gas + dust), including that of dust depletion, ionisation effects and nucleosynthesis effects.

Dust depletion is the phenomenon whereby metals are incorporated into dust grains and are no longer observable in the gas phase (Field 1974; Phillips et al. 1982; Jenkins et al. 1986; Savage & Sembach 1996; Jenkins 2009; De Cia et al. 2016, 2021; Roman-Duval et al. 2021; Konstantopoulou et al. 2022). The depletion of different metals correlates with each other to varying degrees depending on how easily they form dust. The tendency of a metal to deplete into dust is called its refractory index and it is broadly correlated to the condensation temperature of the metal (Savage & Sembach 1996; De Cia et al. 2016; Konstantopoulou et al. 2022). Metals that form dust more readily are referred to as refractory, while those that form dust less easily are volatile. The measure of the relative abundances between metals with different refractory properties is therefore a measurement of the amount of dust depletion. In this method for characterising

dust depletion, called the 'relative method' (De Cia et al. 2016, 2021; Konstantopoulou et al. 2022), the determination of the refractory indices of metals is based on the relative abundances of Zn and Fe. An advantage of the relative method is that it does not make any assumption on the metallicity of the gas.

Other than dust depletion, there are at least two other phenomena that can affect the abundances of metals: ionisation and nucleosynthesis effects. In general, the ions that live in the warm neutral ISM of the Milky Way are singly ionised (with the exception of O I), and are not highly susceptible to further ionisation because they are protected from ionising radiation by neutral hydrogen H I. Elements that are further ionised from ionisation potentials higher than that of H I (13.6eV) can also survive in H II regions, which could result in their apparent over-abundance. For example, as shown in Jenkins (2009), the second ionisation potential of S is higher than that of most other elements, meaning that it can be present in a broader range of H II regions (i.e. where the radiation field is harder and many other elements will be doubly ionised), so it is more likely for it to have contributions from H II regions than most other singly ionised species. Nucleosynthesis effects, for example α -element enhancement and Mn under-abundance, may also affect observed metal abundances. Although α -element enhancements are observed in the Magellanic Clouds (De Cia et al. 2024) and in distant gas-rich galaxies (Velichko et al. 2024), they are not generally seen in the Milky Way.

In most cases, chemical enrichment and metallicities in the neutral ISM are determined for the whole line of sight towards stellar targets in the Milky Way (e.g. Jenkins 2009; De Cia et al. 2021; Ritchey et al. 2023). It is possible that intricacies at smaller scales, i.e. at the level of individual gas components along the lines of sight, make the ISM more complex at this level, and that studying whole lines of sight overlooks small-scale chemical variations. Evidence for this comes from deviations from the normal abundance patterns (the distribution of the observed $[X/H] = \log \frac{N(X)}{N(H)} - \log \frac{N(X_\odot)}{N(H_\odot)}$ against their refractory index for different metals). In these cases, volatile elements seem to deviate from the more typical linear shape of abundance patterns. A possible explanation for these abnormal abundance patterns is that the gas along the lines of sight is a mix of low- and high-depletion and/or metallicity.

With high-resolution absorption-line spectroscopy it is possible to dissect lines of sight, and identify and study the chemical properties of individual gas components (Welty et al. 2020; Ramburuth-Hurt et al. 2023). This allows for a more comprehensive analysis of the variation (if any) in chemical enrichment between different gas clouds along lines of sight. A limitation of the component-by-component analysis is that it is not possible to know the H column density for individual components due to the Lyman- α line being damped, and therefore too broad for the separation of individual components. This means it is not possible to directly measure the metallicity of individual components $[M/H]_i$. It is still possible to characterise the chemical enrichment of individual components using dust depletion as a proxy (e.g. Welty & Crowther 2010; Ramburuth-Hurt et al. 2023). However, although the level of dust depletion has some dependence on metallicity, it also depends on the physical conditions like temperature and density. In high pressure, high density and low temperature gas, such as in the Milky Way disk, the production of molecules and dust has a smaller dependence on metallicity (Blitz & Rosolowsky 2006; Balashev et al. 2017). This means that the distribution of dust depletion does not fully

trace that of the metallicity (Draine 2003; Mattsson et al. 2014; Blitz & Rosolowsky 2006; Balashev et al. 2017).

In this work, we study the dust depletion in individual gas components along eight lines of sight in the Solar neighbourhood with high-resolution UV spectra from HST/STIS. We present a novel methodology of investigating and constraining the metallicities for these individual components using simulations based on hydrogen gas fraction combinations. This paper is organised as follows: Section 2 introduces the data employed in this investigation, Section 3 elaborates on our methodology, Section 4 presents and discusses the findings of this study, and Section 5 summarises the conclusions drawn from our work.

2. Data

In this work, we study the ISM along the lines of sight towards eight bright O/B-type stars within 1.1 kpc of the Sun. These targets are a sub-sample of the 25 targets compiled by De Cia et al. (2021). We select the sub-sample based on three main criteria:

1. The presence of multiple components in the Ti II absorption lines, based on spectra from VLT/UVES and Kitt Peak.
2. An upturn of volatile elements in the abundance patterns in De Cia et al. (2021) which suggests a mix of gases of different dust depletion and/or metallicities along the line of sight.
3. Lower metallicity (≤ -0.16 dex according to De Cia et al. 2021) over the integrated line of sight.

While it is possible that the metallicities from De Cia et al. (2021) are underestimated with respect to other strategies (Ritchey et al. 2023), we based our sample selection on lines of sight that potentially showed signatures of low metallicity gas, which is the motivation for the third condition. The star type, distance from the Galactic center calculated from Gaia data release 3 (GR3), galactic latitude (b) and longitude (l), and the extinction (A_V) for the eight targets are included in Table 1.

2.1. HST data

The data we use in this work are primarily from the high spectral resolution ($R \sim 114\,000$) HST/STIS program ID:16750 of the eight bright O/B stars within 1.1 kpc of the Sun. This program had 15 orbits in two settings: E140H with a central wavelength of 1271 Å, covering 1170 – 1372 Å, and E230H with a central wavelength of 2113 Å covering 1974 – 2251 Å. In the case of ρ Oph A, HD 206267 and HD 207198, the spectra for the E230H/2113 setting already exists in the archive. Table A.1 contains observational details of this program including the number of orbits, exposure time and signal-to-noise ratio (SNR) for each setting. The wavelength bands were chosen to include the absorption lines for a number of transitions of interest tabulated in Table 2. We use the 1D spectra directly from the archive, which have been reduced by the standard CALSTIS pipeline.

2.2. Auxiliary data

We made use of the following data to supplement the absorption lines listed above. Specifically, because the decomposition of the lines is important for this work, the supplementary very high-resolution data are used to determine the substructure of the absorption lines.

- Archival high-resolution HST/STIS spectra ($R \sim 114\,000$, FWHM ~ 2.63 km/s) that cover the Fe II $\lambda\lambda$ 2260, 2367

Table 1: Target information with distances from the Galactic center calculated using Gaia DR3. The A_V values are taken from Valencic et al. (2004).

Target	HD	Type	Galactocentric distance (kpc)	Heliocentric distance (pc)	l ($^\circ$)	b ($^\circ$)	A_V
θ^1 Ori C	37022	O6-7p	8.6 ± 0.2	399 ± 21	209.0	-19.4	1.78 ± 0.36
HD 110432	110432	B0.5IVpe	8.1 ± 0.2	438 ± 14	302.0	-0.2	-
ρ Oph A	147933	B2IV	8.2 ± 0.2	137 ± 2	353.7	17.7	2.58 ± 0.34
χ Oph	148184	B2IVpe	8.1 ± 0.2	152 ± 4	357.9	20.7	-
HD 154368	154368	O9Ia	7.2 ± 0.2	1064 ± 38	350.0	3.2	2.53 ± 0.20
κ Aql	184915	B0.5III _n	7.9 ± 0.2	506 ± 39	31.8	-13.3	-
HD 206267	206267	O6.0V((f))+O9:V	8.4 ± 0.2	735 ± 118	99.2	3.7	1.47 ± 0.14
HD 207198	207198	O9IIe	8.6 ± 0.2	1002 ± 34	103.1	7.0	1.50 ± 0.29

lines for the targets ρ Oph A, HD 206267 (ID:16285) and HD 207198 (ID:9465).

- VLT/ESPRESSO spectra (ID:0102.C-0699(A), $R \sim 190\,000$, FWHM ~ 1.54 km/s) that cover Ca II $\lambda\lambda$ 3934, 3969, K I $\lambda\lambda$ 7664, 7698, and Na I $\lambda\lambda$ 5889, 5895.
- Kitt Peak National Observatory (KPNO) spectra from the Coude Feed Telescope with Camera 6 ($R \sim 220\,000$, FWHM ~ 1.35 km/s) that cover Ca II λ 3934 and K I $\lambda\lambda$ 7664, 7698, and from the Coude Feed Telescope with Camera 5 ($R \sim 88\,000$, FWHM ~ 3.4 km/s) that covers Ti II λ 3384.
- McDonald spectra ($R \sim 176\,000$, FWHM ~ 1.7 km/s) that cover K I $\lambda\lambda$ 7664, 7698 and Ca II $\lambda\lambda$ 3934, 3969 (Pan et al. 2004).
- UHRF spectra covering Na I $\lambda\lambda$ 5889, 5895, K I λ 7698 (Welty & Hobbs 2001) and Ca II $\lambda\lambda$ 3934, 3969 ($R \sim 880\,000$, FWHM ~ 0.34) (Price et al. 2001).
- VLT/UVES spectra (ID:194.C-0833, $R \sim 92\,600$, FWHM ~ 3.2 km/s) that cover Ti II $\lambda\lambda\lambda$ 3230, 3242, 3384.

Table 2 contains the lab wavelengths, oscillator strengths and γ values for each of the transitions we consider here.

3. Methodology

To analyse the chemical enrichment and variations along these lines of sight, we start with measuring column densities using Voigt-profile fitting software packages, described in Section 3.1. In this work, we go beyond the more typical study of the abundance patterns (variations of $[X/H]$ with the refractory index) along the full line of sight by performing a component-by-component analysis along the lines of sight. To do this, we construct metal patterns (also called depletion patterns in Ramburuth-Hurt et al. 2023). These are the metal-to-metal variations with respect to their tendency to deplete onto dust grains, namely the refractory indices, plotted against their equivalent metal column densities ($\log N(X) - \log N(H)$ for a given metal X). From these metal patterns we can pinpoint the amount of dust depletion in individual components (Section 3.2). We then perform simulations, based on the observations, to further constrain the possible ranges of metallicities of the individual components (Section 3.3). We do this by exploring many distributions of the total hydrogen gas among the components. In this section, we describe this methodology in more detail and discuss some of its caveats.

3.1. Measuring column densities

The H I column densities are measured from the Lyman- α absorption line at 1215 Å by determining the radial velocity for

Ion	Transition wavelength (Å)	Oscillator strength	Reference
Ni II	1317.217	0.0596	[1]
Cr II	2056.2568	0.11	[2]
Cr II	2062.2343	0.078	[3]
Cr II	2066.161	0.0515	[3]
Fe II	2249.8754	0.00182	[3]
Fe II	2260.7791	0.00244	[3]
Mn II	1197.1843	0.205	[3]
Mn II	1199.3912	0.16	[3]
Mn II	1201.1177	0.115	[3]
Ge II	1237.0591	1.230	[3]
Si II	1260.4221	1.45	[3]
Si II	1304.3702	0.106	[3]
Mg II	1239.9253	0.000633	[3]
Mg II	1240.3947	0.000355	[3]
S II	1250.578	0.0052	[3]
S II	1253.805	0.01	[3]
S II	1259.518	0.016	[3]
Zn II	2026.137	0.63	[2]
Zn II	2062.6604	0.31	[2]
P II	1301.8743	0.0196	[4]
O I	1302.168	0.052	[3]
O I	1355.5977	0.0000116	[3]
Ca II	3934.777	0.65	[3]
Ca II	3969.591	0.32	[3]
Ti II	3230.1219	0.0773	[3]
Ti II	3242.9181	0.233	[3]
Ti II	3384.73	0.353	[3]

Table 2: Table of the lab wavelengths, oscillator strengths and their reference for the transitions considered in this work. [1] Boissé & Bergeron (2019), [2] Cashman et al. (2017), [3] Morton (2003), [4] Brown et al. (2018)

most of the gas from the O I λ 1355 line. This is a good indicator of the velocity structure of H I because its ionisation energy is very similar to that of H I and the ionisation fractions of O I and H I are strongly coupled to each other by a charge exchange process with a large rate coefficient (Stancil et al. 1999; Spirko et al. 2004). This line is also far from being saturated, and oxygen is not much depleted onto dust grains. The outcome of this velocity measurement is used to establish an origin for the HI absorption profiles. The column density is then measured by determining the best fit damping profile for the Lyman- α line. In some cases, one side of the H I absorption profile showed sufficient cancellation of the H I absorption while the other side exhibited extra absorption. This effect could be due to some absorption by the stellar

Lyman- α if the star's velocity is displaced from that of the foreground gas. It is not easy to confirm this interpretation, however, because there is a high probability that the star could be a spectroscopic binary and therefore could exhibit this same effect. The targets with this effect are θ^1 Ori C, HD 154368, HD 110432, χ Oph. Column densities of H_2 are taken from Savage et al. (1977).

We use two software packages for measuring the metal column densities for the targets in this work. For most of the targets (ρ Oph A, HD 110432, HD 154368, HD 2062676 and HD 207198) we use the Voigt-profile fitting software `VoigtFit` (Krogager 2018). For κ Aql, χ -Oph, θ^1 Ori C, metal column densities are measured using `fits6p` (Welty et al. 1991, 2003, 2020). Note that the uncertainties on the column densities for the fits with `fits6p` are underestimated.

For all targets, the structure of the absorption lines is determined by first fitting the lines covered by the highest-resolution spectra we have. We do this in order to best capture the intricacies of the line profiles, and because the STIS data are under-sampled (less than 2 pixels per resolution element). We assume that all species have a common velocity structure, which is obtained from the highest resolution spectra, but with possible slight adjustments based on the UV profiles, especially in the cases of weak components or broad lines. We assume that the component absorption lines are represented by symmetric Voigt profiles, and that asymmetry implies the presence of more than one component.

For ρ -Oph A, HD 110432, HD 154368, HD 2062676 we use one (or both simultaneously, when available) of $Ca\ II\ \lambda\lambda 3934, 3969$. For HD 207198, the $Ca\ II$ lines are saturated, and therefore cannot be used. Instead, we fit simultaneously to $Cr\ II\ \lambda\lambda 2056, 2062, 2066$ and $Ti\ II\ \lambda\ 3384$ to determine the structure. For κ Aql, χ Oph and θ^1 Ori C, we obtained a mutually consistent structure from the highest resolution KI, Na I, and $Ca\ II$ spectra that were available. The b -values (which represent the distribution of velocities due to gas turbulence and thermal kinematics, with turbulence dominating in the warm neutral ISM), velocities and column densities for fits to the highest resolution data are included in Table C.1 in Appendix C.

Once the component profile is determined, the decomposition is then assumed to be applicable to all other singly ionised species. The column densities are measured using all available (non-saturated, non-contaminated) lines from the same species according to this structure. In several cases, there is a velocity offset between the optical and UV spectra, which is taken into account when applying the velocity structure across these spectra. The spectra and fits are shown in Appendix C.

For some of the ions, it is not possible to decompose their absorption lines to the same level of intricacy as the high resolution lines either because the lines are weaker, because of blending at lower resolution, or for both of these reasons. As a result, and to ensure the reliability of our measurements, we consider the column densities of groups of components (grouped by velocity) rather than all components individually, also because these are generally more well-constrained than individual components. It is important to note that the decomposition of components is not necessarily physical, and we do not know if the separation in velocity space means that they are separated in physical space. In this work, we are careful to group the components using the highest-resolution spectra to identify individual components. Tables C.2 – C.9 in Appendix C present the column densities for groups of components, including the way that the components were grouped and their respective velocity ranges. For simplicity and to avoid repetitive phrasing, we use the term *components*

to refer to groups of gas components for the remainder of this paper.

$S\ II$, $Si\ II$ and $Zn\ II$ are often saturated. We do not use the $S\ II$ and $Si\ II$ lines in our analysis because of their severe saturation, and do not use $Zn\ II$ for HD 206267 and HD 207198. Some of the components on the edges of the $Zn\ II$ absorption lines are salvageable, and we take the column densities from `VoigtFit` to be lower limits on the total line of sight. When there are individual components on the edges of the $Zn\ II$ profiles that are unsaturated, we include these in the component-by-component analysis.

Most of the absorption lines towards ρ Oph A are saturated (see the fits in Fig. G.3). We can recover reliable column densities for the first component only, but the lines for the second group of components (group 2, components 4 – 7) are too saturated, with the exception of $Ti\ II$ and $O\ I$. Therefore, for this target, we only take into account $Ti\ II$ and $O\ I$ for the metal pattern of group 2. We do not perform further analysis on this line of sight.

3.2. Dust depletion of individual components

We use the relative method of characterising dust depletion where the depletion of element X , denoted as δ_X , is estimated from relative abundances (De Cia et al. 2016; Konstantopoulou et al. 2022), not observed abundances. Relative abundances are defined as $[X/Y] = \log N(X)/N(Y) - \log N(X)_\odot/N(Y)_\odot$, where the Solar abundances are taken from (Asplund et al. 2021) following the recommendation of (Lodders et al. 2009).

The relative method is based on full line-of-sight measurements along lines of sight in the Milky Way, Magellanic Clouds, GRB- and QSO-DLAs. Here we assume that the method is applicable to the individual components that we study in this paper based on the following. Firstly, Ramburuth-Hurt et al. (2023) demonstrated that the dust depletion sequences hold for individual components in QSO-DLAs, i.e. ionisation effects are limited, and the dominant effect of dust depletion can be clearly identified and studied also in individual components. However, that study did not include Milky Way lines of sight, or systems with a high level of dust depletion. This adds some level of uncertainty to this study. The line of sight towards HD 62542 in the Milky Way (Welty et al. 2020) is an example of a case where the depletion patterns in individual components may depart from the general trends. Evidence for deviations from the linear behaviour of metal patterns would provide clues that this method is not applicable to individual components in this regime. Secondly, dust depletion has been shown to behave similarly in different environments (QSO-, GRB-DLAs, Magellanic Clouds and Milky Way, Konstantopoulou et al. 2022). Finally, the dust tracer $[Zn/Fe]$ correlates with other relative abundances that are used as dust tracers, such as $[Si/Ti]$ (De Cia et al. 2016; Konstantopoulou et al. 2024).

Most extragalactic work is based on the full line-of-sight analysis of mid/high-resolution ($R < 50\ 000$) spectra.

The amount of depletion is expressed as

$$\delta_X = A2_X + B2_X \times [Zn/Fe]_{\text{fit}}, \quad (1)$$

where $[Zn/Fe]_{\text{fit}}$ is a measure of the overall strength of depletion, or the depletion factor; $A2_X$ and $B2_X$ are coefficients of the depletion sequence fits in Konstantopoulou et al. (2022) and are specific for each element (see Table 3). $B2_X$ is the refractory index, which represents the ease with which a metal is captured onto dust grains. Refractory elements form dust relatively readily and have more negative $B2_X$ values, while volatile elements

do not form dust so easily and have less negative $B2_X$ values. Note that $A2_X$ is typically consistent with zero within the uncertainties, and in principle it could be assumed to be equal to zero.

In general, we define the total dust-corrected metallicity of a metal X as

$$[X/H]_{\text{tot}} = [X/H] - \delta_X, \quad (2)$$

where $[X/H]_{\text{tot}}$ represents the total metallicity of the neutral ISM, including dust and gas, and $[X/H]$ are the observed gas-phase abundances. For i individual gas components along a line of sight, we combine these two equations to obtain

$$y_i = a_i + B2_X \times [Zn/Fe]_{i,\text{fit}}, \quad (3)$$

which is a linear relation, $y_i = a_i + bx$, where

$$y_i = \log N(X)_i - X_\odot + 12 - A2_X, \quad (4)$$

$$a_i = [M/H]_i + \log N(H)_i. \quad (5)$$

Here, $\log N(X)_i$, $[M/H]_i$ and $\log N(H)_i$ are the metal column density, dust corrected metallicity and total hydrogen (i.e. $H\text{ I} + H_2$, IGNORING THE IONISED HYDROGEN $H\text{ II}$) column density for individual gas components along the line of sight. y_i represents the ‘normalised’ (by its Solar abundance) metal column densities.

We plot the y_i values for each metal against its corresponding $B2_X$, which constitutes what we call a ‘metal pattern’ (or ‘depletion pattern’ in Ramburuth-Hurt et al. 2023) In the case where there is no dust depletion (or any other causes of deviation), y_i for each metal would be similar. If there is only dust depletion at play, we would expect the y_i values to align on a straight line with a gradient $[Zn/Fe]_{\text{fit},i}$, which represents the overall strength of depletion. The y -intercept of this straight line, $a_i = [M/H]_i + \log N(H)_i$, is the sum of the total hydrogen column density and dust-corrected metallicity of the individual gas component, and it is degenerate. To demonstrate this degeneracy, consider a line of sight with two individual components and the following two (of several possible) scenarios. If we have $a_1 < a_2$, it is possible for component 2 to either have the majority of the hydrogen and a low metallicity or it could have less hydrogen but a higher metallicity than component 1.

With the relative method, we characterise the level of dust depletion for individual gas components along the line of sight regardless of its hydrogen content. Deviations from the fitted linear relation are possible and could be due to processes such as ionisation or nucleosynthesis (e.g. α -element enhancement), or peculiar depletion due to local physical conditions of a gas cloud. Potential peculiarities of dust depletion were observed for the Magellanic Clouds (Jenkins & Wallerstein 2017), but are likely due to α -element enhancement (Konstantopoulou et al. 2022; De Cia et al. 2024). The relative method is able to distinguish between dust depletion, α -element enhancement and metallicity variations.

An alternative to the relative method is the F^* method (Jenkins 2009). We do not discuss this method in this paper, but the values for depletion we determine here are related to the F^* method by the equation $F^* = 1.05 \times [Zn/Fe]_{\text{fit}} - 0.86$ (based on data from De Cia et al. 2021).

While the metallicity of components is not possible to constrain, the dust depletion of each component is well-constrained by Equation 3. Metal patterns give us information on any variation in the amount of dust between gas clouds along a line of sight. We are able to study the dust depletion of the ISM on a component-by-component basis without making assumptions on the metallicity or the hydrogen distribution.

Table 3: Coefficients of the depletion sequences for metals X (Konstantopoulou et al. 2022). The values for P are those from Konstantopoulou et al. (2023).

δ_X	$A2_X$	$B2_X$
δ_{Zn}	0.00 ± 0.01	-0.27 ± 0.03
δ_O	0.00 ± 0.00	-0.20 ± 0.05
δ_P	0.08 ± 0.05	-0.26 ± 0.08
δ_S	0.01 ± 0.02	-0.48 ± 0.04
δ_{Si}	-0.04 ± 0.02	-0.75 ± 0.03
δ_{Mg}	0.01 ± 0.03	-0.66 ± 0.04
δ_{Ge}	0.00	-0.40 ± 0.04
δ_{Mn}	0.07 ± 0.02	-1.03 ± 0.03
δ_{Cr}	0.12 ± 0.01	-1.30 ± 0.01
δ_{Fe}	-0.01 ± 0.03	-1.26 ± 0.04
δ_{Ti}	-0.07 ± 0.03	-1.67 ± 0.04

3.3. Simulating clouds: exploring the metallicities of individual gas components

It can be argued that the distribution of $O\text{ I}$ can be used to give some insight into the distribution of hydrogen, both because it traces $H\text{ I}$ (due to their similar ionisation potential), and because it is not highly depleted into dust. The caveat with using the $O\text{ I}$ gas fraction as a direct tracer of the hydrogen fraction is that it makes the assumption that the metallicity of each gas component is the same. We choose not to do this here in order to avoid this assumption.

The distinctive difference between metal patterns described here and the more typical abundance patterns (the study of the observed abundances of elements with different refractory properties) is that we do not know the hydrogen column densities for individual components. Therefore, metals patterns cannot directly provide the metallicity of the component.

In order to investigate possible metallicities for components along our lines of sight, we perform simulations. The simulations take into account the observed column densities and then explore possible hydrogen gas distributions between the components. In practice, we use the y -intercept a_i derived from the linear fit to the metal patterns, and calculate the metallicity based on different combinations of hydrogen gas fractions. Rewriting Equation 5 gives

$$[M/H]_i = a_i - \log(f_i \times N(H)_{\text{tot}}). \quad (6)$$

Here, $N(H)_{\text{tot}}$ is the total hydrogen column density along the full line of sight, which can also be written in terms of the gas fraction:

$$N(H)_i = f_i \times N(H)_{\text{tot}}, \quad (7)$$

such that $\sum_i f_i = 1$.

The hydrogen gas fraction combinations are generated as follows. In general, for m number of whole integers that add up to 100, the number of combinations is $= \binom{100-1}{m-1} = \frac{(100-1)!}{(m-1)!100!}$. Here, we first generate all these possible permutations for each number of components, i.e. $m = 2, 3, 4, 5$. We then generate all the permutations of these and remove any duplicates. This process produces over three million combinations for $m = 5$, therefore, to optimise subsequent calculations, we randomly sample 1 000 000 combinations from these, where 1 000 000 is chosen because it yields enough combinations to cover the parameter space between 0% – 100% in intervals of 1%. For 2 to 4 components, we obtain 99, 4 851, 156 849, combinations respectively,

which is visualised in Fig. 1. The aim of this procedure is to have combinations that span the parameter space in intervals of 1%.

Then, for each gas fraction combination, we calculate the corresponding set of metallicities from Equation 6, which we also refer to as a realisation. We do this for each combination of gas fractions and for each target. This gives us the possible ranges of metallicities for the components along each line of sight. In principle, each realisation is equally likely.

To investigate the minimum possible range in metallicity along each line of sight, we compute the difference between the maximum and minimum metallicity for each realisation, and extract the realisation that produces the minimum difference. We interpret this as the minimum possible variation in metallicity.

We test this methodology by combining our observations towards HD 206267 with a sight line towards the SMC, which has known metallicity and $\log N(\text{H I})$ from De Cia et al. (2024), to create a synthetic sight line. The choice of an SMC sight line is to demonstrate that our method can distinguish between the low metallicity of the SMC and the higher metallicity of the Milky Way. The test confirms that we are able to recover a 0.6 dex difference in metallicity between both the Milky Way components and the SMC (i.e. $[\text{M}/\text{H}]_{\text{MW1}} - [\text{M}/\text{H}]_{\text{SMC}} > 0.6$ and $[\text{M}/\text{H}]_{\text{MW2}} - [\text{M}/\text{H}]_{\text{SMC}} > 0.6$) for 5 out of 4865 most-likely realisations. These 5 realisations also recover the metallicity and hydrogen gas fraction of the SMC cloud. The complete test is detailed in Appendix B.

4. Results and discussion

From the analysis of the metal patterns, we derive the dust depletion of individual components and calculate the range in dust depletion along each of the eight lines of sight as the difference between the maximum and minimum depletion. We generally do not see strong evidence of deviations from the linear behaviour of the metal patterns of the individual components in this sample, and therefore assume that the relative method can be applied here. One exception to this may be the case of θ^1 Ori C, where a potential overabundance of the iron-group elements or underabundance of TiII is observed.

We find ranges up to 1.19 dex in one case and present these results in Section 4.1. Using simulations, we further explore the possible metallicities and gas fractions of the individual components, which can be constrained to 0.1 dex for some lines of sight. The simulation results are presented in Section 4.2. We analyse the realisation that produces the minimum range in metallicity for each sight line in Section 4.3. In Section 4.4 we present the abundance patterns along the full lines of sight.

4.1. Variations in dust depletion

In our component-by-component analysis, some components show very high levels of dust depletion. The highest level of dust depletion we find is $[\text{Zn}/\text{Fe}]_{\text{fit},i} = 2.03 \pm 0.03$ dex (or $F^* = 1.5$) for group 3 in χ Oph. This value is larger than the maximum dust depletion reported by De Cia et al. (2021), which is 1.32 dex, observed towards ι Ori. Here we show the metal pattern for χ Oph in Fig. 2. In Table 4 we present $[\text{Zn}/\text{Fe}]_{\text{fit},i}$ and a_i for each component along each sight line. The metal patterns for the remaining targets are presented in Appendix D.

We also observe a large range in dust depletion along sight lines. Fig. 3 shows that, for four of our sight lines, the difference between maximum and minimum $[\text{Zn}/\text{Fe}]_{\text{fit},i}$ values reaches ~ 1.0 dex. For most targets, several components have significantly

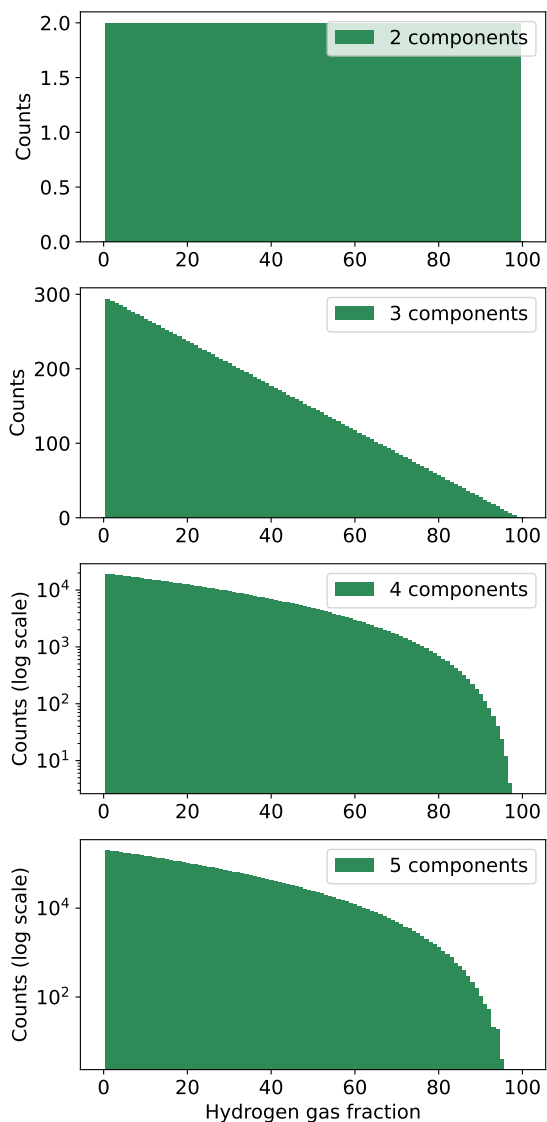


Fig. 1: The distributions of total hydrogen gas fractions that we use to infer the metallicities of individual components. From the top to the bottom panel are the distributions for 2 to 5 components respectively. The histograms for 4 and 5 components are plotted in log-scale for visual clarity.

higher or lower levels of dust depletion compared to that of the total sight line. This result confirms that total line-of-sight analyses (e.g. De Cia et al. 2021; Ritchey et al. 2023) can wash out the level of diversity in depletion along sight lines. Indeed, it is consistent with established variations in $[\text{Na}/\text{Ca}]$ in many Milky Way sight lines (Routly & Spitzer 1952; Siluk & Silk 1974) and with the few studies of individual components (Fitzpatrick & Spitzer 1994; Welty et al. 2020).

In Fig. 4 we plot the velocity ranges of the groups of components against their depletion. This is to investigate, firstly, any relationship between kinematics and the depletion, and secondly, any trends that could be associated with the Local Bubble (Lallement et al. 2003; Zucker et al. 2022). The Local Bubble is a pocket of plasma with low density and high temperature in which the Sun sits. Outside of the Bubble is a shell of cold, neutral gas. Zucker et al. (2022) find that several of the nearby star-forming regions sit on the edge of the Local Bubble, at a velocity of 6.7

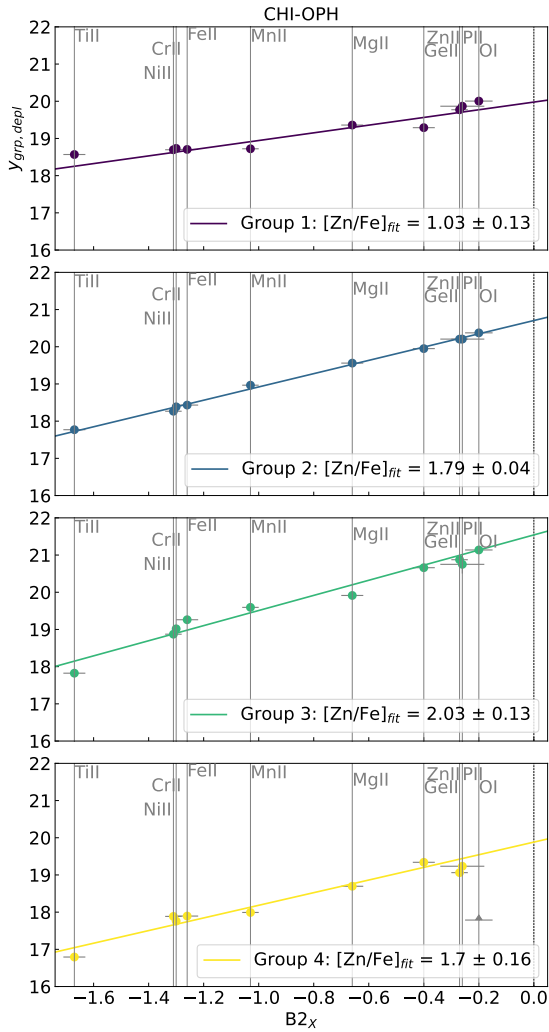


Fig. 2: Metal patterns for grouped components towards χ Oph. This line of sight has the highest value for dust depletion out of our sample, with $[\text{Zn}/\text{Fe}]_{\text{fit},3} = 2.03 \pm 0.13$ dex.

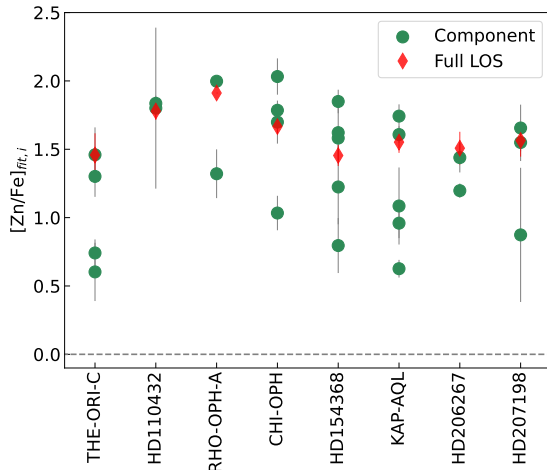


Fig. 3: Depletion factors for individual components along each line of sight are represented by green points. The $[\text{Zn}/\text{Fe}]_{\text{fit}}$ values for the entire line of sight are plotted as red diamonds.

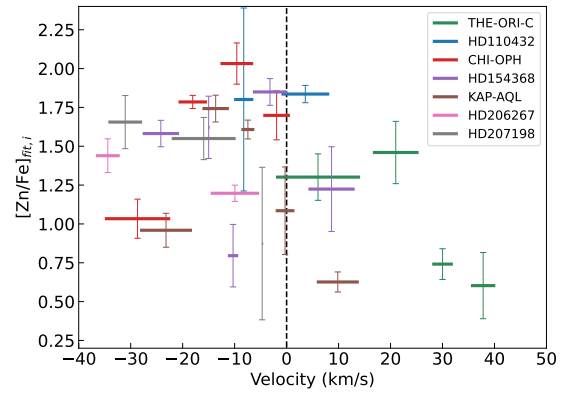


Fig. 4: Velocity-depletion plot for groups of components.

Table 4: Results from the metal patterns. The values in square brackets are based on a fit to only two points, and are therefore not reliable.

Target	Group	$[\text{Zn}/\text{Fe}]_{i,\text{fit}}$	$a_{i,\text{depl}}$
θ^1 Ori C	1	1.30 ± 0.15	20.07 ± 0.12
	2	1.46 ± 0.20	21.65 ± 0.22
	3	0.74 ± 0.10	19.26 ± 0.10
	4	0.60 ± 0.21	18.67 ± 0.29
HD 110432	1	1.80 ± 0.59	20.15 ± 0.73
	2	1.84 ± 0.06	21.57 ± 0.07
ρ Oph A	1	1.32 ± 0.18	20.15 ± 0.19
	2	[2.0]	[22.02]
χ Oph	1	1.03 ± 0.13	19.98 ± 0.12
	2	1.79 ± 0.04	20.71 ± 0.04
	3	2.03 ± 0.13	21.58 ± 0.18
	4	1.70 ± 0.16	20.02 ± 0.20
HD 154368	1	1.58 ± 0.08	20.44 ± 0.08
	2	1.62 ± 0.20	20.27 ± 0.23
	3	0.80 ± 0.20	20.18 ± 0.25
	4	1.85 ± 0.09	21.60 ± 0.10
	5	1.22 ± 0.27	20.04 ± 0.35
κ Aql	1	0.96 ± 0.11	19.6 ± 0.11
	2	1.74 ± 0.09	21.16 ± 0.01
	3	1.60 ± 0.06	20.56 ± 0.06
	4	1.09 ± 0.28	19.32 ± 0.34
	5	0.63 ± 0.06	19.33 ± 0.07
HD 206267	1	1.41 ± 0.07	20.01 ± 0.08
	2	1.2 ± 0.05	21.26 ± 0.07
HD 207198	1	1.25 ± 0.25	20.7 ± 0.29
	2	1.55 ± 0.14	21.49 ± 0.17
	3	0.87 ± 0.49	19.71 ± 0.68

± 0.45 km/s, like the Orion region. We do not find any significant relationship between velocity and depletion, or any patterns, for example systematic α -element enhancement of components around 6.7 km/s, that could be associated with the Local Bubble. Fig. 4 agrees well, however, with the velocity-depletion results of Routly & Spitzer (1952) and Siluk & Silk (1974). There may be a slight anti-correlation between absolute velocity and the level of dust depletion in these works, although we remain uncertain about the potential causes. (Routly & Spitzer 1952; Siluk & Silk 1974) interpret this as evidence for the partial destruction of dust grains within velocities of ~ 40 km/s, possibly due to SNe shocks.

4.2. Variations in metallicity

The simulations we perform produce thousands of possible metallicity combinations for individual gas components based on hydrogen gas fraction combinations, as described in Section 3.3. From these simulations we obtain the possible ranges of metallicities for each component (see Fig. 5 for χ Oph results). In principle, all of the realisations are equally possible because we do not state any preference for particular hydrogen gas fraction combinations. However, we do make a physically motivated upper cut on possible metallicities, which narrows the range of their possible values. The threshold is based on the maximum metallicity found in stars in the Milky Way’s disk, which Nepal et al. (2024) find to be 0.4 dex. To be conservative, we assume that the upper limit on the gas-phase metallicity could be slightly higher and therefore impose a limit of $[M/H]_i \leq 0.5$ dex. This limit decreases the range of allowed metallicities for most components, and can even constrain the possible metallicity of a component down to within an interval of ~ 0.3 dex including uncertainties, for example group 3 of χ Oph and group 2 of HD 110432. We show the allowed metallicities for each component along our lines of sight in Appendix D (Figures E.2 – E.5). The highlighted points in these figures indicate the realisation that produces the smallest range in metallicity. This is discussed later in Section 4.3.

In five lines of sight (θ^1 Ori C, χ Oph, HD 154368, κ Aql, HD 207198), we find that the component with the highest $[Zn/Fe]_{fit,i}$ holds the majority of the hydrogen gas, and also likely has super-Solar metallicity. These five cases and these results are listed in Table 5. The exceptions are ρ Oph A, for which we cannot perform this analysis due to limited data, and HD 110432 and HD 206267, which both have two components of the same $[Zn/Fe]_{fit,i}$ within the uncertainties. Below we further discuss the results of the most-likely realisations for some of the targets.

4.2.1. θ^1 Ori C

In addition to group 2 having high depletion, this component has super-Solar metallicity and the bulk of the hydrogen gas (see Fig. 6). Additionally, there is evidence that this gas cloud is attributed to the gas Orion nebula itself (Price et al. 2001). We also find that group 4 has the lowest amount of dust depletion, sub-Solar metallicity, and $\leq 40\%$ of the hydrogen gas.

4.2.2. HD 110432

The two components along this line of sight have similar depletion: $[Zn/Fe]_{fit,1} = 1.80 \pm 0.59$ and $[Zn/Fe]_{fit,2} = 1.84 \pm 0.06$ (see Fig. E.1). Although the metallicity of group 2 can be constrained to be $\geq 0.40 \pm 0.19$ dex, we cannot constrain the metallicity for group 1 to the same degree. Our simulations show that it is possible for the two components to have similar depletion but have vastly different metallicities. For example, one realisation for these two components produces $[M/H]_1 = -0.39 \pm 0.12$ and $[M/H]_2 = 0.50 \pm 0.12$, which is a difference of ~ 0.89 dex.

4.2.3. ρ Oph A

It is not possible to draw any conclusions about metallicity variations along this line of sight due to lack of data.

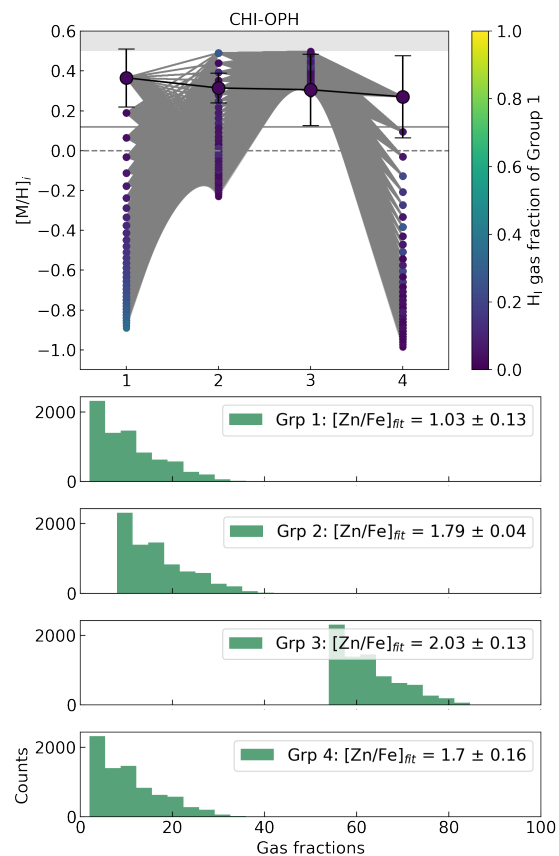


Fig. 5: The simulation realisations for the most-likely cases (where the metallicities for all groups are ≤ 0.5 dex) for χ Oph. The solid grey horizontal line in the top panel represents the metallicity along the whole line of sight, taking into account all of the metals. The points with black edge colours connected by the black line highlight the case with the minimum differences in metallicity. The grey-shaded region above 0.5 dex shows the upper bound criteria for the metallicities. The colours of the points correspond to the gas fraction of the first group $N(H_1)$ for each realisation (i.e. approximately $1\% \leq f_1 \leq 45\%$), and is represented by the colour bar. The histograms in the following panels are the total hydrogen gas fractions, f_i for the most-likely cases. We include the level of dust depletion $[Zn/Fe]_{fit,i}$ in the legends.

4.2.4. χ Oph

The simulations for this line of sight constrain the gas fractions for each group within a range of $\sim 30\%$, with group 3 having the majority of the gas (55% – 85%, see Fig. 5). This line of sight has the component with the highest depletion of all our targets: $[Zn/Fe]_{fit,4} = 2.03 \pm 0.13$, which we also constrain to have super-Solar metallicity $[M/H]_4 \geq 0.3$.

4.2.5. HD 206267

The groups along this line of sight appear to be similar in terms of depletion, gas fractions and metallicity (see Fig. E.4). Gas fractions overlap significantly, making it more difficult to disentangle the degeneracy between metallicity and hydrogen gas fraction. It is possible that the gas we probe along this line of sight is chemically homogeneous, also considering that we found the minimum difference in metallicities to be zero.

Table 5: Table showing the five sight lines where the component with the highest depletion also contains the majority of the hydrogen gas. For χ Oph and κ Aql, we find that the metallicities of these components are also constrained to super-Solar.

Target	Group	$[\text{Zn}/\text{Fe}]_{\text{fit},i}$	f_i	$[\text{M}/\text{H}]_i \geq$
θ^1 Ori C	2	1.46 ± 0.20	$37\% < f_2 < 97\%$	0.08 ± 0.31
χ Oph	3	2.03 ± 0.13	$54\% < f_3 < 88\%$	0.29 ± 0.21
HD 154368	4	1.85 ± 0.09	$38\% < f_4 < 89\%$	0.13 ± 0.25
κ Aql	2	1.74 ± 0.09	$43\% < f_2 < 84\%$	0.20 ± 0.15
HD 207198	2	1.55 ± 0.14	$39\% < f_2 < 77\%$	0.20 ± 0.21

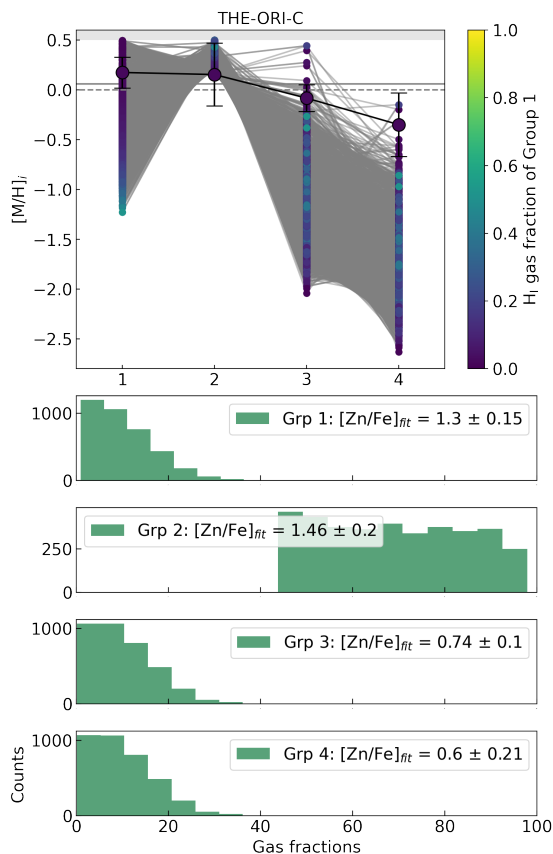


Fig. 6: The same as Fig. 5, but for θ^1 Ori C.

4.3. Minimum differences in metallicity

Here we report and analyse the realisations that produce the smallest difference in metallicity for each line of sight. As described in Section 3.3, this realisation is as equally likely as each other realisation in principle. We interpret it as the minimum possible level of variation in metallicity. The metallicities and gas fractions of these realisations are tabulated in Table 6 for all sight lines. The uncertainties here are propagated from the fits to the metal patterns and the uncertainties in $N(\text{H})_{\text{tot}}$. In Figures 5 and E.2 – E.5 these ‘minimum-difference’ realisations are highlighted by the larger points and joined with a black solid line.

For HD 110432 and HD 206267, both with two components, we find the difference in metallicity to be zero. For the remaining lines of sight, the difference in metallicity is between 0.02 and 1.02 dex.

For χ Oph, HD 110432 and HD 154368 we find that the metallicities in the minimum-difference case are all higher than that for the total line of sight (indicated by the solid grey line).

While the likelihood is, in principle, the same as others, this discrepancy may suggest that these are not highly likely options.

We find that the gas fractions for the minimum-difference realisations are on the extreme ends, only below $\sim 20\%$ or above $\sim 70\%$, shown in Fig. 9. This means that, in order to have \sim the same metallicity in all components along the line of sight, one of the components has to carry the vast majority of the hydrogen gas.

We perform a statistical z -test to quantify how significant the difference in metallicity is when considering the uncertainties:

$$z = \frac{([\text{M}/\text{H}]_{\text{max}} - [\text{M}/\text{H}]_{\text{min}})}{\sqrt{\Delta[\text{M}/\text{H}]_{\text{min}}^2 + \Delta[\text{M}/\text{H}]_{\text{max}}^2}}, \quad (8)$$

where $[\text{M}/\text{H}]_{\text{max}}$ and $[\text{M}/\text{H}]_{\text{min}}$ are the maximum and minimum metallicities, and $\Delta[\text{M}/\text{H}]_{\text{max}}$ and $\Delta[\text{M}/\text{H}]_{\text{min}}$ are their respective uncertainties. A z -value above 3 means that the difference between the maximum and minimum metallicities is statistically significant to the 3σ level.

The line of sight towards θ^1 Ori C has the most statistically significant difference in metallicity, although it is still small with only 2.5σ . The results from this exercise are tabulated in Table 7. In Fig. 7, we plot these minimum differences in metallicity against the difference in dust depletion $[\text{Zn}/\text{Fe}]_{\text{fit}}$, and do not find any strong correlation.

Fig. 8 shows the minimum differences in metallicity for our lines of sight compared to the positions of the targets with respect to the Sun. This is to investigate whether the length of the line of sight (i.e. the distance from Earth to the target star) has an impact on the amount of variation in metallicity. We do not find any coherent spatial variation linked to the metallicity variations.

It is important to point out that small shifts in the gas fractions can produce drastically different ranges in metallicity and result in the metallicities. For example, the minimum difference between the two groups of components for HD 110432 gives gas fractions of $f_1 = 4\%$ and $f_2 = 96\%$ and metallicities of $[\text{M}/\text{H}]_1 = 0.37 \pm 0.85$ and $[\text{M}/\text{H}]_2 = 0.41 \pm 0.19$. However, if we move $\sim 10\%$ of the gas from component 2 to component 1 so that they become $f_1 = 13\%$ and $f_2 = 86\%$, then the range in metallicity increases to 0.6 dex with $[\text{M}/\text{H}]_1 = -0.15 \pm 0.85$ and $[\text{M}/\text{H}]_2 = 0.45 \pm 0.19$.

4.4. Abundance patterns for the whole line of sight

Fig. 10 shows the abundance patterns for full lines of sight (i.e. combining all velocity components) towards our κ Aql. The remaining targets are included in Appendix F. We perform three different linear fits for most of the targets: (1) fits to all the metals (red dashed line), (2) fits to only the more refractory metals (Ti II, Ni II, Cr II, Fe II, Mn II) in purple, and (3) fits to only the more volatile metals (Mg II, Ge II, Zn II, P II, O I) in green. We define a limit between more refractory and more volatile elements around a value of $B_{2\chi} \sim 0.8$. For ρ Oph A we report the fit to

Table 6: The metallicities and corresponding gas fractions for the cases with the minimum difference in metallicity.

Target	Group	$[M/H]_i$	f_i (%)
θ^1 Ori C	1	0.00 ± 0.15	3
	2	0.10 ± 0.31	95
	3	-0.33 ± 0.13	1
	4	-0.92 ± 0.32	1
HD 110432	1	0.37 ± 0.85	4
	2	0.41 ± 0.19	96
χ Oph	1	0.37 ± 0.15	2
	2	0.31 ± 0.07	12
	3	0.31 ± 0.18	84
	4	0.27 ± 0.21	2
HD 154368	1	0.22 ± 0.23	5
	2	0.15 ± 0.38	4
	3	0.18 ± 0.40	3
	4	0.14 ± 0.25	86
	5	0.22 ± 0.50	2
κ -Aql	1	0.27 ± 0.27	2
	2	0.23 ± 0.24	76
	3	0.30 ± 0.22	20
	4	0.29 ± 0.30	1
	5	0.30 ± 0.30	1
HD 206267	1	-0.12 ± 0.12	6
	2	-0.10 ± 0.11	94
HD 207198	1	0.28 ± 0.33	35
	2	0.28 ± 0.21	61
	3	0.30 ± 0.72	4

Table 7: Table of the minimum and maximum metallicities and their respective z -test significance for the minimum-difference realisation.

Target	Min. $[M/H]_i$	Max. $[M/H]_i$	Diff. (dex)	z -test (σ)
θ^1 Ori C	-0.92 ± 0.32	0.10 ± 0.15	1.02	2.5
HD110432	0.37 ± 0.19	0.41 ± 0.85	0.04	0
χ Oph	0.27 ± 0.37	0.30 ± 0.07	0.10	0.4
HD154368	0.14 ± 0.25	0.22 ± 0.23	0.08	0.2
κ Aql	0.23 ± 0.1	0.30 ± 0.13	0.07	0.5
HD206267	-0.12 ± 0.12	-0.10 ± 0.11	0.02	0.1
HD207198	0.28 ± 0.72	0.28 ± 0.33	0	0

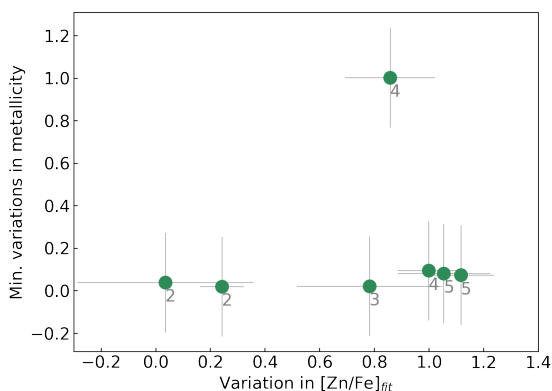


Fig. 7: Variation in $[Zn/Fe]_{fit}$ plotted against the minimum difference in metallicity for all targets. The grey numbers indicate the number of groups of components along the line of sight.

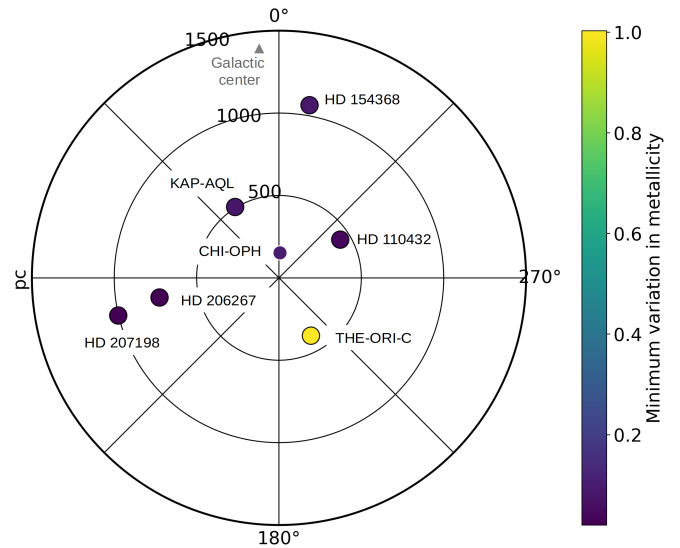


Fig. 8: Labelled target map, colour-coded by the minimum differences in metallicity based on our realisations. The Sun is positioned at the center.

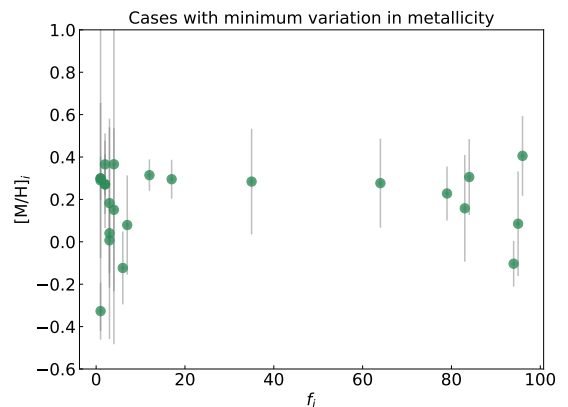


Fig. 9: Plot of metallicity realisations for individual components as a function of their gas fraction for the cases with minimum difference in metallicity. Here we see that these cases require the gas fractions to be either very high or very low.

the only two reliable column densities. For θ^1 Ori C we only include results from the fit to all metals and to the more volatile because we find the fit to the more refractory metals yields unreliable results. This could be caused by Fe-group (Ni, Cr, Fe, Mn) over-abundance in this ISM cloud, or by peculiar Ti depletion (which is also seen in lines of sight towards other stars in this region Ritchey et al. 2023). In general, it is clear that the abundance pattern fits to all the metals are not linear, and that there is an upturn of the more volatile metals. This is likely due to the presence of a mix of gases along the lines of sight with different levels of depletion, and possibly different metallicities.

The purpose of performing linear fits to only the refractory/volatile elements is to show that we find that these two strategies measure different metallicities for the same lines of sight. For a given abundance pattern, fits to only the more refractory metals systematically produce lower metallicities, while fits to only the more volatile metals result in metallicities that are more similar to fits to all the metals. If low-metallicity gas exists along the line of sight, the refractory metals are the only ones

sensitive to it because the volatile elements are always dominated by the omnipresent high-metallicity gas. On the other hand, the refractory elements are mostly highly depleted in the high-metallicity gas, and their abundance can instead be dominated by the low-depletion, low-metallicity gas. It is also possible to have high metallicity gas and low dust content, for example due to dust destruction. However, our approach is agnostic to metallicity because we directly measure the dust depletion of individual components, without assumptions on the metallicity. We may expect the presence of low-metallicity gas in the ISM because there is evidence of accreting low-metallicity gas, for example from HVCs (Fox & Davé 2017).

Table 8 summarises these results. In Fig. 11 we compare our results with those from De Cia et al. (2021); Ritchey et al. (2023). We include the metallicity gradient based on H II regions from Arellano-Córdova et al. (2020).

These results confirm that using abundance patterns to calculate the metallicity of gas along full lines of sight is an approximation, and that component-by-component analyses are important for gaining a holistic measurement of the chemical enrichment in the ISM.

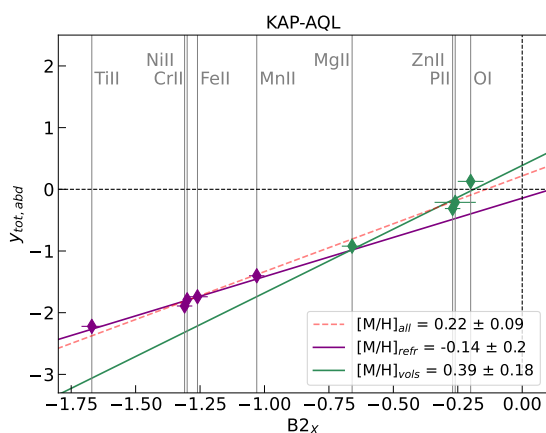


Fig. 10: Abundance pattern for the total line of sight towards κ Aql. The red dashed line shows the fit to all of the metals, the purple is the fit to the more refractory metals, and the green is fit to the more volatile.

5. Conclusions

In this work we study individual (groups of) components along eight lines of sight within 1.1 kpc of the Sun. We use metal patterns and the relative method to determine the amount of dust depletion $[Zn/Fe]_{fit,i}$ in each component. We investigate possible metallicities for these individual components by simulating 99, (4 851, 156 849, 1 000 000) distributions of the total hydrogen gas between 2 (3, 4, 5) components. Our results are summarised below.

1. We find components with very high levels of dust depletion (up to $[Zn/Fe]_{fit} = 2.03 \pm 0.03$ dex or $F^* = 1.30$) compared to the full line-of-sight analysis conducted by De Cia et al. (2021), who report a maximum depletion of 1.32 or $F^* = 0.53$. Our study shows that full line-of-sight analyses can wash out the range of dust depletion. This means that it is possible to have much higher levels of depletion in individual clouds compared to the full line of sight.
2. We find large ranges in the level of dust depletion among components along lines of sight, calculated as the difference between the minimum and maximum depletion, up to 1.19 dex.
3. We present a novel method of constraining the metallicities of individual gas components. We use information gained from the metals patterns, i.e. that the y -intercept is the sum of the hydrogen gas fraction and the metallicity $a_i = \log N(H)_i + [M/H]_i$, with simulated $\log N(H)_i$ distributions to calculate $[M/H]_i$ for individual components. We implement an upper metallicity limit of 0.5 dex based on results from Nepal et al. (2024). From our simulations and under this assumption, we are able to constrain metallicities for some components to be within an interval of ~ 0.3 dex.
4. Our simulations indicate that, in five out of eight lines of sight, the component with the highest level of dust depletion contains the majority of the hydrogen gas, and likely has super-Solar metallicity.
5. For the line of sight towards θ^1 Ori C, we find a group of components (group 2 out of 4 groups) with high dust depletion $[Zn/Fe]_{fit,2} = 1.52 \pm 0.25$, the bulk of the hydrogen gas $37\% < f_2 < 97\%$, and super-Solar metallicity $[M/H]_2 \geq 0.08$ dex. This group of components could be attributed to the nebula itself (Price et al. 2001). Further, we find that group 4 has a low level of depletion $[Zn/Fe]_{fit,4} = 0.60 \pm 0.21$, and likely low metallicity, at least for the case with the minimum difference in metallicity.
6. From our realisations, we find that the minimum variation in metallicity is < 0.15 dex for all targets, with the exception of θ^1 Ori C, which we find to be 1.02 dex. Although the metallicity of individual gas components cannot be strictly measured, this methodology allows us to study the minimum variations of metallicity, from component to component.

With the methodology we develop in this paper to constrain the metallicities of individual gas clouds in the Solar neighbourhood, we are able to study the ISM in more detail, and we gain a better understanding of the level of chemical variation in the ISM.

Acknowledgements. Edward B. Jenkins passed away just before the submission of this paper. Ed was one of the great fathers of UV astronomy and his scientific work on the ISM was immensely impactful and inspiring. We are grateful to have had the opportunity to work with and learn from him. His legacy will live on. Daniel E. Welty calculated the column densities for the targets θ^1 Ori C, χ Oph and κ Aql. The authors acknowledge and thank him for his significant and valuable contributions to this paper. T.R.-H., A.D.C., J.-K.K., C.K. and A.V. acknowledge support by the Swiss National Science Foundation under grant 185692. This work is based on observations with the NASA/ESA Hubble Space Telescope obtained from Mikulski Archive for Space Telescopes at the Space Telescope Science Institute, which is operated by the Association of Universities for Research in Astronomy, Incorporated, under NASA contract NAS5-26555. We also make use of optical data from the European Southern Observatory, Kitt Peak National Observatory, McDonald Observatory and the Anglo-Australian Telescope. Support for program number 16750 was provided through a grant from the STScI to Princeton University and STScI under NASA contract NAS5-26555. This research has made use of NASA's Astrophysics Data System.

References

- Arellano-Córdova, K. Z., Esteban, C., García-Rojas, J., & Méndez-Delgado, J. E. 2020, MNRAS, 496, 1051
Asplund, M., Amarsi, A. M., & Grevesse, N. 2021, A&A, 653, A141
Balashev, S. A., Noterdaeme, P., Rahmani, H., et al. 2017, MNRAS, 470, 2890
Blitz, L. & Rosolowsky, E. 2006, ApJ, 650, 933
Boissé, P. & Bergeron, J. 2019, A&A, 622, A140
Brown, M. S., Alkhayat, R. B., Irving, R. E., et al. 2018, ApJ, 868, 42

Target	No. comps	Groups of comps	[M/H] _{tot}	[Zn/Fe] _{fit,tot}	[M/H] _{ref}	[M/H] _{vol}	[M/H] _{DC21}	[M/H] _{R23 all metals}
θ^1 Ori C	16	4	0.06 ± 0.20	1.46 ± 0.20	–	0.20 ± 0.10	-0.50 ± 0.20	–
HD 110432	6	2	0.36 ± 0.07	1.78 ± 0.06	0.19 ± 0.27	[0.43]	-0.14 ± 0.15	–
ρ Oph A	15	2	[0.36]	[1.91]	–	–	-0.78 ± 0.12	-0.036 ± 0.094
χ Oph	19	4	0.12 ± 0.06	1.66 ± 0.06	0.1 ± 0.19	0.36 ± 0.07	-0.33 ± 0.11	–
HD 154368	11	5	-0.02 ± 0.08	1.45 ± 0.08	-0.42 ± 0.2	-0.06 ± 0.23	-0.42 ± 0.12	–
κ Aql	16	5	0.22 ± 0.09	1.60 ± 0.07	-0.14 ± 0.2	0.37 ± 0.18	-0.22 ± 0.14	–
HD 206267	7	2	0.16 ± 0.14	1.51 ± 0.12	-0.55 ± 0.3	0.44 ± 0.31	-0.21 ± 0.12	-0.097 ± 0.067
HD 207198	6	2	0.27 ± 0.14	1.56 ± 0.12	-0.66 ± 0.13	0.52 ± 0.21	-0.67 ± 0.08	-0.05 ± 0.067

Table 8: Results from the abundance patterns for each target. We include the metallicities calculated over the full lines of sight obtained from only fitting to the refractory metals and only fitting to the volatile metals, as well as a comparison to the literature. [M/H]_{DC21} and [M/H]_{R23} are metallicities from De Cia et al. (2021) and Ritchey et al. (2023) respectively. The values in square brackets are from fits done to only two data points.

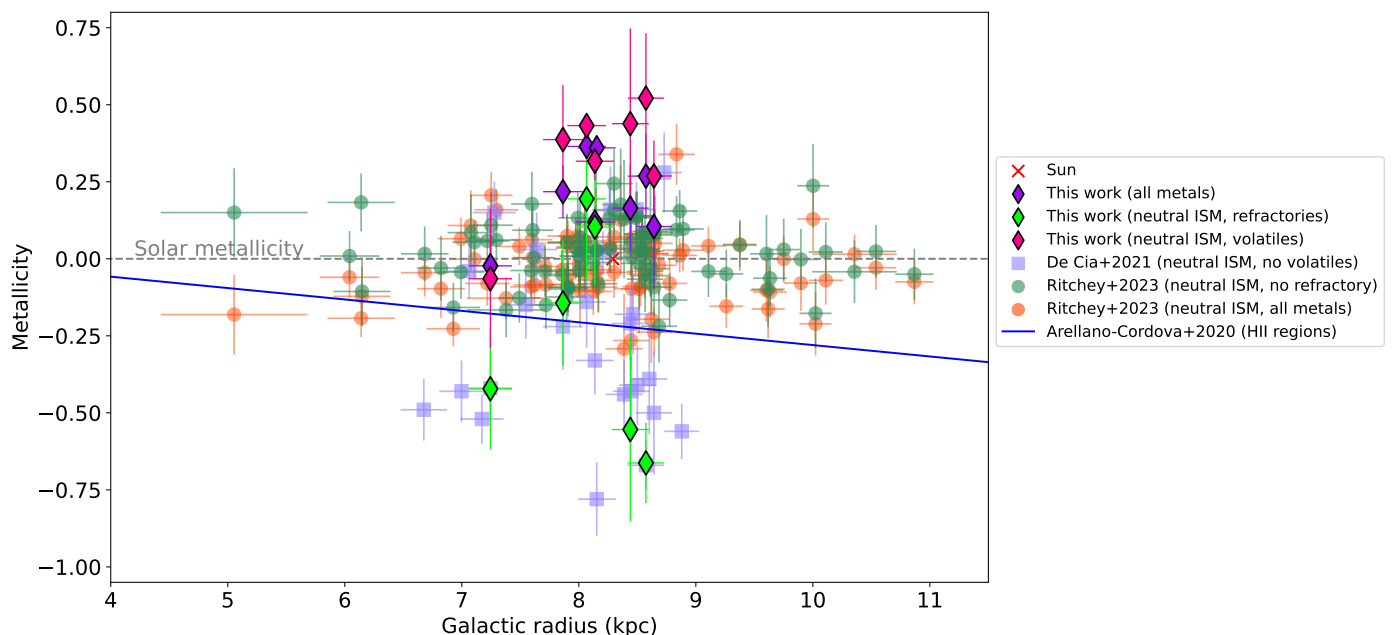


Fig. 11: Metallicity calculated over the full lines of sight as a function of distance from the Galactic center plotted for this work compared with literature results. The red diamonds are the results from the fit to abundance patterns for all metals, the green and purple diamonds are fits to the refractory and volatile metals respectively. We do not include the fits for ρ Oph A because of the limited data. The fit to the refractory metals for θ^1 Ori C is 1.7, which we do not consider as physical, so it is excluded in this plot.

- Cashman, F. H., Kulkarni, V. P., Kisielius, R., Ferland, G. J., & Bogdanovich, P. 2017, VizieR Online Data Catalog: Compilation of atomic data for key heavy elements (Cashman+, 2017), VizieR On-line Data Catalog: J/ApJS/230/8. Originally published in: 2017ApJS..230....8C
- Crain, R. A., Schaye, J., Bower, R. G., et al. 2015, MNRAS, 450, 1937
- De Cia, A., Jenkins, E. B., Fox, A. J., et al. 2021, Nature, 206
- De Cia, A., Ledoux, C., Mattson, L., et al. 2016, A&A, 596, A97
- De Cia, A., Roman-Duval, J., Konstantopoulou, C., et al. 2024, A&A, 683, A216
- Draine, B. T. 2003, ARA&A, 41, 241
- Field, G. B. 1974, ApJ, 187, 453
- Fitzpatrick, E. L. & Spitzer, Lyman, J. 1994, ApJ, 427, 232
- Fox, A. & Davé, R. 2017, Gas Accretion onto Galaxies
- Fox, A. J., Richter, P., Ashley, T., et al. 2019, ApJ, 884, 53
- Jenkins, E. B. 2009, ApJ, 700, 1299
- Jenkins, E. B., Savage, B. D., & Spitzer, L. 1986, ApJ, 301, 355
- Jenkins, E. B. & Wallerstein, G. 2017, ApJ, 838, 85
- Konstantopoulou, C., De Cia, A., Krogager, J.-K., et al. 2022, A&A, 666, A12
- Konstantopoulou, C., De Cia, A., Krogager, J.-K., et al. 2023, A&A, 674, C1
- Konstantopoulou, C., De Cia, A., Krogager, J.-K., et al. 2024, A&A, 691, A129
- Krogager, J.-K. 2018, VoigtFit: Absorption line fitting for Voigt profiles, Astrophysics Source Code Library, record ascl:1811.016
- Lallement, R., Welsh, B. Y., Vergely, J. L., Crifo, F., & Sfeir, D. 2003, A&A, 411, 447
- Lodders, K., Palme, H., & Gail, H. P. 2009, Landolt BÖrstein, 4B, 712
- Mattsson, L., De Cia, A., Andersen, A. C., & Zafar, T. 2014, MNRAS, 440, 1562
- Morton, D. C. 2003, ApJS, 149, 205
- Nelson, D., Pillepich, A., Springel, V., et al. 2019, MNRAS, 490, 3234
- Nepal, S., Chiappini, C., Guiglion, G., et al. 2024, A&A, 681, L8
- Pan, K., Federman, S. R., Cunha, K., Smith, V. V., & Welty, D. E. 2004, VizieR Online Data Catalog: Optical spectra in star-forming regions (Pan+, 2004), VizieR On-line Data Catalog: J/ApJS/151/313. Originally published in: 2004ApJS..151..313P
- Péroux, C., Nelson, D., van de Voort, F., et al. 2020, MNRAS, 499, 2462
- Phillips, A. P., Gondhalekar, P. M., & Pettini, M. 1982, MNRAS, 200, 687
- Pillepich, A., Nelson, D., Springel, V., et al. 2019, MNRAS, 490, 3196
- Price, R. J., Crawford, I. A., Barlow, M. J., & Howarth, I. D. 2001, MNRAS, 328, 555
- Ramburuth-Hurt, T., De Cia, A., Krogager, J. K., et al. 2023, A&A, 672
- Richter, P. 2017, in Astrophysics and Space Science Library, Vol. 430, Gas Accretion onto Galaxies, ed. A. Fox & R. Davé, 15
- Ritchey, A. M., Jenkins, E. B., Shull, J. M., et al. 2023, ApJ, 952, 57
- Roman-Duval, J., Jenkins, E. B., Tchernyshyov, K., et al. 2021, ApJ, 910, 95
- Routly, P. M. & Spitzer, Lyman, J. 1952, ApJ, 115, 227
- Savage, B. D., Bohlin, R. C., Drake, J. F., & Budich, W. 1977, ApJ, 216, 291
- Savage, B. D. & Sembach, K. R. 1996, ARA&A, 34, 279
- Schaye, J., Crain, R. A., Bower, R. G., et al. 2015, MNRAS, 446, 521

- Siluk, R. S. & Silk, J. 1974, *ApJ*, 192, 51
- Spirko, J. A., Neiman, M. L., Oelker, A. M., & Klier, K. 2004, *Surface Science*, 572, 191
- Stancil, P. C., Schultz, D. R., Kimura, M., et al. 1999, *A&AS*, 140, 225
- Valencic, L. A., Clayton, G. C., & Gordon, K. D. 2004, *ApJ*, 616, 912
- Velichko, A., De Cia, A., Konstantopoulou, C., et al. 2024, *A&A*, 685, A103
- Welty, D. E. & Crowther, P. A. 2010, *MNRAS*, 404, 1321
- Welty, D. E. & Hobbs, L. M. 2001, *ApJS*, 133, 345
- Welty, D. E., Hobbs, L. M., & Morton, D. C. 2003, *ApJS*, 147, 61
- Welty, D. E., Hobbs, L. M., & York, D. G. 1991, *ApJS*, 75, 425
- Welty, D. E., Sonnentrucker, P., Snow, T. P., & York, D. G. 2020, *ApJ*, 897, 36
- Zucker, C., Goodman, A. A., Alves, J., et al. 2022, *Nature*, 601, 334

6

Appendix A: Details of observations

Table A.1 shows the details of the HST/STIS cycle 29 observations (ID: 16750) used in this work.

Appendix B: Methodology test

We test our methodology described in Section 3 by adding an extra component with known metallicity and total hydrogen column density to the line of sight towards HD 206267. This component, chosen from the SMC, helps us verify that our method can accurately recover the metallicity difference between the Milky Way and the SMC. We use data from De Cia et al. (2024) for AzV 78, who report $[Zn/Fe]_{\text{fit}} = 0.62 \pm 0.12$, $[M/H] = -0.82 \pm 0.17$ and $\log N(H) = 21.7 \pm 0.06$. We choose the sight line towards HD 206267 because it has only two components with relatively low dust depletion, reducing the degeneracy between the components. This makes the hydrogen gas fraction for the SMC component $f_{\text{SMC}} = 74\%$.

For 5 out of the 4865 most likely realisations (i.e. metallicities of all components are < 0.5 dex) from this exercise, we recover a difference in metallicities of > 0.6 dex between both Milky Way clouds and the SMC (i.e. $[M/H]_{\text{MW1}} - [M/H]_{\text{SMC}} > 0.6$ dex and $[M/H]_{\text{MW2}} - [M/H]_{\text{SMC}} > 0.6$ dex). These realisations also reproduce the SMC metallicity of -0.82 ± 0.17 . There is one realisation that produces a difference of 0.8 dex, and none produce larger than this. In the former case the SMC metallicity is also reproduced. Fig. B.1 shows the 5 realisations with metallicity differences > 0.6 dex in the green points and the 1 realisation that produces a difference of > 0.8 dex in purple, plotted over all of the ‘most likely’ realisations in grey (see Section 4.2). The metallicity of the SMC cloud is shown by the horizontal dotted black line. The gas fraction histogram in the bottom panel shows that this exercise somewhat reproduces the SMC gas fraction.

Appendix C: Voigt fits and column densities

In Table C.1 we present the b -values, velocities and column densities from the Voigt fits to the highest resolution data which we used to determine the absorption-line structure. Tables C.2 – C.9 present the column densities for individual (groups of) components for each line of sight in this study. The tables include which components are grouped and their relevant velocities. The values in square brackets are lower limits. The dash (–) indicates that the component could not be constrained for that ion.

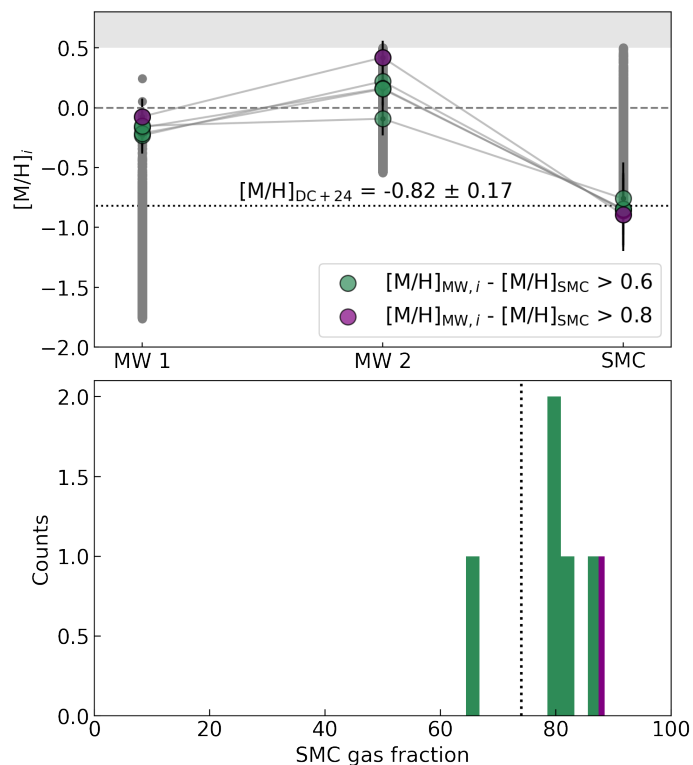


Fig. B.1: Results from testing of our method in Section 3.3 showing we reproduce the large range in metallicity between the Milky Way and the SMC for 5 out of the 4865 realisations. In the top panel we plot all of the ‘most-likely’ realisations in grey and over-plot those which recover a 0.6 dex difference in metallicity between both of the Milky Way clouds and the SMC cloud in green. The histogram in the bottom panel shows the total hydrogen gas distributions for these realisations.

Target	Orbits E140H/1271	Aperture	Exposure time (s)	Max. SNR	Orbits E230H/2113	Aperture	Exposure time (s)	Max. SNR
θ^1 Ori C	1	31X0.05NDB	1786	48	1	31X0.05NDC	2508	65
HD 110432	1	0.1X0.03	2828	74	1	0.1X0.03	2040	52
χ Oph	1	31X0.05NDB	2536	49	1	31X0.05NDA	1866	49
ρ Oph A	–	–	–	–	1	0.2X0.06	1786	59
HD 154368	2	0.2X0.2	5395	21	2	0.2X0.2	5143	20
κ Aql	1	31X0.05NDB	2508	61	1	31X0.05NDA	1786	53
HD 206267	–	–	–	–	1	6X0.2	2018	33
HD 207198	–	–	–	–	1	6X0.2	2030	41

Table A.1: Table of the observing details for HST cycle 29 program ID: 16750. The reported maximum SNR is per pixel. Additional archival data are used in this work as described in Section 2.

Table C.1: Voigt parameters for the highest-resolution lines that we used for the structure of the absorption lines. For seven of the targets Ca II was used, with the exception of HD 207198 where Ti II was used. Where the b -values or velocities do not have associated uncertainties, it means that these parameters were fixed in the fitting process.

Target	Ion	Component	b -value (km/s)	error	velocity (km/s)	error	logN(X)	error
θ^1 Ori C	Ca II	1	2.00		-2.05	0.54	10.09	0.012
		2	1.40		0.53	0.24	10.25	0.012
		3	4.00		6.57	0.07	11.46	0.013
		4	0.80		10.09	0.24	10.17	0.015
		5	1.30		12.07	0.28	10.59	0.013
		6	1.00		14.14	0.19	10.55	0.015
		7	1.40		16.60	0.10	11.00	0.011
		8	0.71		18.67	0.09	10.69	0.013
		9	1.10		20.57	0.03	11.22	0.013
		10	0.77		23.34	0.03	11.04	0.009
		11	1.00		25.40	0.08	10.7	0.008
		12	1.00		28.02	0.08	10.79	0.01
		13	0.80		29.95	0.04	11.14	0.012
		14	0.89		31.99	0.02	11.47	0.016
		15	1.80		35.47	0.15	10.46	0.007
		16	2.50		40.16	0.13	10.66	0.008
HD 110432 [†]	Ca II	1	1.8		-10.1		10.1	0.422
		2	1.2		-6.4		9.46	1.326
		3	6.5		-1		10.76	0.215
		4	3.1		5.2		11.56	0.043
		5	0.9		5.8		11.59	0.035
		6	2.4		8.2		11.42	0.033
ρ Oph A [†]	Ca II	1	3.4		-29.2		10.54	0.061
		2	5.8		-20.4		10.36	0.121
		3	0.8		-13.4		10.38	0.056
		4	2.9		-10.1		10.77	0.06
		5	1.5		-8.3		12.1	0.007
		6	0.3		-7.2		13.15	0.033
		7	1.0		-0.3		9.99	0.125
χ Oph	Ca II	1	1.4		-31.52	0.14	10.37	0.007
		2	1.5		-28.20	0.06	11.06	0.012
		3	1.6		-25.31	0.08	11.1	0.012
		4	1.4		-22.39	0.15	10.91	0.016
		5	1.0		-20.80	0.06	10.2	0.037
		6	0.7		-19.77	0.06	10.13	0.024
		7	0.6		-19.02	0.06	9.77	0.017
		8	1.2		-17.84	0.06	10.45	0.01
		9	1.2		-15.33	0.06	10.4	0.007
		10	0.9		-12.73	0.06	10.87	0.014
		11	0.8		-11.40	0.06	10.87	0.05
		12	0.9		-10.56	0.06	11.48	0.043
		13	1.0		-8.64	0.06	11.27	0.02
		14	0.9		-7.39	0.06	<10.26	
		15	1.0		-6.43	0.06	10.43	0.015
		16	0.6		-4.49	0.10	10.2	0.007
HD 154368 [†]	Ca II	1	1.7		-27.7		10.46	0.127
		2	1.8		-20.7		11.54	0.024
		3	0.8		-15		11.42	0.037
		4	2.3		-11.3		10.51	0.315
		5	13.5		-9.3		12.23	0.024
		6	0.3		-6.5		10.72	0.447
		7	2.3		-4.5		12.24	0.028
		8	2.1		0.1		11.42	0.039
		9	10.3		4.2		10.51	0.873
		10	2.7		7.7		11.73	0.022
		11	0.6		13.1		9.93	0.325

Continued on next page

Target	Ion	Component	b -value (km/s)	error	velocity (km/s)	error	logN(X)	error
κ Aql	Ca II	1	1.5	0.1	-28.2	0.1	10.41	0.008
		2	0.9		-21.8	0.1	10.61	0.008
		3	1.5		-18.2	0.2	10.64	0.016
		4	0.8		-16.2	0.1	11.16	0.019
		5	1.3		-13.5	0.1	11.75	0.056
		6	1.3		-11.1	0.1	11.69	0.045
		7	1.4		-8.7	0.1	11.39	0.031
		8	1.5		-6.2	0.1	11.21	0.027
		9	2.0		-2.1	0.1	10.93	0.012
		10	1.7		1.5	0.1	11.12	0.012
		11	2.5		5.8	0.1	11.3	0.027
		12	2.6		10.0	0.1	11.85	0.029
		13	2.5		13.9	0.1	11.2	0.027
HD 206267 [†]	Ca II	1	2		-32.1		10.89	0.018
		2	4.9		-26.7		11.79	0.004
		3	2		-14.6		11.62	0.013
		4	6.6		-13.8		12.1	0.006
		5	3		-8.2		12.4	0.008
		6	1.9		-3.2		11.3	0.018
		7	7.1		-5.3		11.81	0.012
HD 207198 ^{†, a}	Ti II	1	7		-27.8		10.54	0.511
		2	2.9		-22.1		10.44	0.398
		3	3.3		-16.8		11.69	0.029
		4	2		-13		11.46	0.05
		5	2.1		-9.8		11.58	0.033
		6	1.6		-4.7		11.35	0.041

[†] Fitting done with VoigtFit. The remaining lines of sight were fit using fits6p.

^a An additional component at ~ 34 km/s is possibly observed only for Zn II but not for other ions. It is not clear whether this component is physical or due to contamination.

Appendix D: Metal patterns

Here we include the metal patterns for the targets not included in the main text.

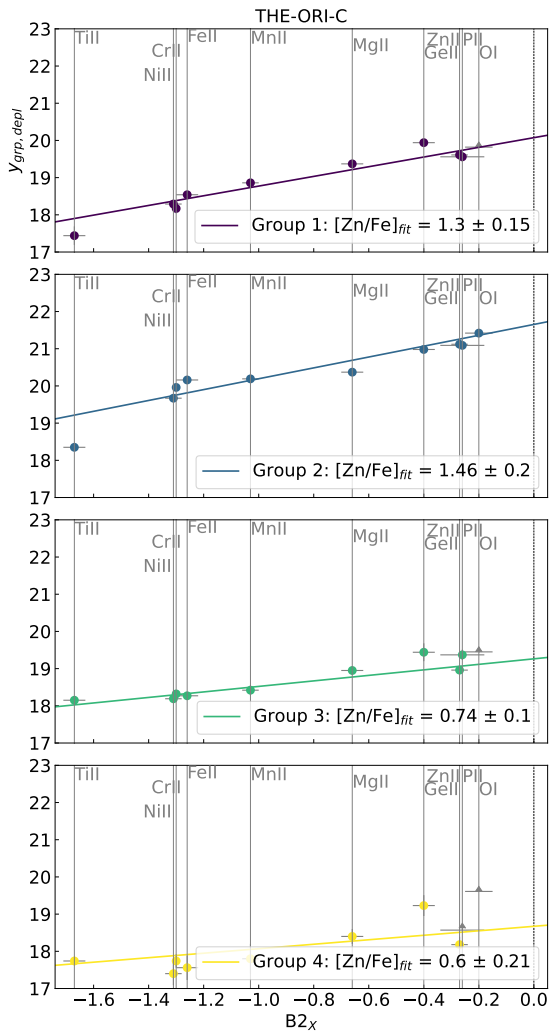


Fig. D.1: Metal patterns for grouped components towards θ^1 Ori C.

Appendix E: Most-likely realisations

Here we include the most-likely realisations for the targets not included in the main text.

Appendix F: Abundance pattern plots

The abundance patterns for the targets not included in the main text are shown here.

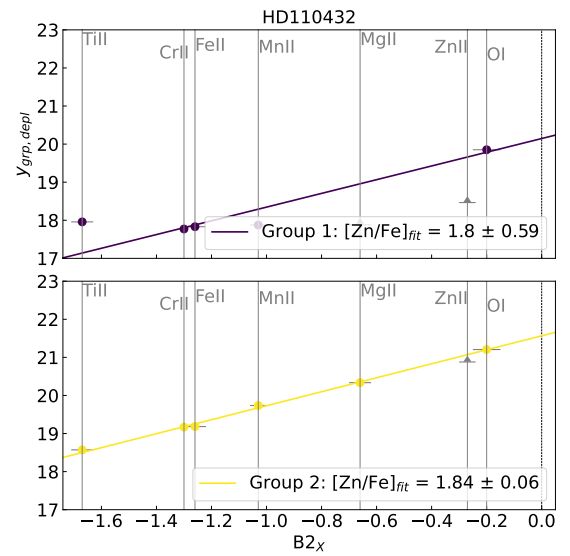


Fig. D.2: Metal patterns for grouped components towards HD 110432.

Appendix G: Fits to spectra

Figures G.1 to G.7 are the Voigt fits to the spectra for each target.

Table C.2: Column densities for θ^1 Ori C in logarithmic scale, determined using the Voigt-profile fitting software fits6p. We include the way in which individual components are grouped, and their relevant velocity ranges. H_{tot} is the sum of H I determined in this work and H_2 from Savage et al. (1977)

. The total column densities in square brackets indicate that these lines are saturated, and the reported value is a lower limit. These measurements are not used in our analysis.

Ion	Total	Group 1 Comps 1 – 6 [−2.05, 14.14] km/s	Group 2 Comps 7 – 11 [16.6, 25.4] km/s	Group 3 Comps 12 – 14 [28.02, 31.99] km/s	Group 4 Comps 15 – 16 [35.47, 40.16] km/s
H_{tot}	21.59 ± 0.10				
H I	21.59 ± 0.03				
H_2	17.25 ± 0.1				
Ca II	12.16 ± 0.03	11.61 ± 0.01	11.68 ± 0.01	11.69 ± 0.01	10.87 ± 0.02
Cr II	13.73 ± 0.02	11.92 ± 0.12	13.71 ± 0.02	12.07 ± 0.07	11.49 ± 0.17
Fe II	15.63 ± 0.03	13.99 ± 0.04	15.61 ± 0.03	13.72 ± 0.07	13.01 ± 0.30
Ge II	12.64 ± 0.02	11.54 ± 0.10	12.58 ± 0.02	11.04 ± 0.24	10.83 ± 0.28
Mg II	15.98 ± 0.01	14.92 ± 0.04	15.92 ± 0.01	14.5 ± 0.08	13.95 ± 0.17
Mn II	13.76 ± 0.03	12.4 ± 0.06	13.73 ± 0.03	11.96 ± 0.12	11.34 ± 0.38
Ni II	13.98 ± 0.01	12.56 ± 0.07	13.94 ± 0.02	12.46 ± 0.06	11.67 ± 0.29
O I	18.13 ± 0.02	< 17.00	18.11 ± 0.01	< 16.83	< 16.75
P II	14.61 ± 0.01	13.06 ± 0.08	14.59 ± 0.01	12.87 ± 0.09	< 12.48
Ti II	11.48 ± 0.03	10.27 ± 0.22	11.18 ± 0.04	10.98 ± 0.07	10.57 ± 0.06
Zn II	13.75 ± 0.04	12.22 ± 0.02	13.73 ± 0.04	11.57 ± 0.05	10.79 ± 0.20

Table C.3: Column densities for HD 110432 in logarithmic scale, determined using the Voigt-profile fitting software VoigtFit.

Ion	Total	Group 1 Comps 1 – 2 [−10.1, −6.4] km/s	Group 2 Comps 3 – 6 [−1.0, 8.2] km/s
H_{tot}	21.18 ± 0.10		
H I	21.03 ± 0.03		
H_2	20.64 ± 0.10		
Ca II	12.04 ± 0.027	10.19 ± 1.936	12.03 ± 0.05
Cr II	12.94 ± 0.022	11.52 ± 0.015	12.92 ± 0.008
Ti II	11.5 ± 0.006	10.79 ± 0.002	11.4 ± 0.002
Fe II	14.65 ± 0.011	13.28 ± 0.026	14.63 ± 0.005
Mg II	15.89 ± 0.007	[13.43]	15.89 ± 0.003
Mn II	13.28 ± 0.014	11.42 ± 0.015	13.28 ± 0.007
O I	17.92 ± 0.016	16.54 ± 0.004	17.9 ± 0.011
Zn II	[13.49]	[11.08]	[13.49]

Table C.4: Column densities for ρ Oph A in logarithmic scale, determined using the Voigt-profile fitting software VoigtFit.

Ion	Total	Group 1 Comps 1 – 2 [−29.2, −20.4] km/s	Group 2 Comps 3 – 7 [−13.4, −0.3] km/s
H_{tot}	21.67 ± 0.10		
H I	21.63 ± 0.03		
H_2	20.57 ± 0.10		
Ca II	13.19 ± 0.03	10.76 ± 0.018	13.19 ± 0.023
Cr II	[15.11]	12.13 ± 0.018	[15.11]
Fe II	[16.94]	13.92 ± 0.009	[16.94]
Mg II	[15.76]	14.75 ± 0.209	[15.7]
Mn II	[14.34]	12.37 ± 0.004	[14.34]
O I	18.33 ± 0.013	16.98 ± 0.001	18.31 ± 0.004
P II	[15.76]	–	[15.76]
Ti II	11.66 ± 0.012	11.12 ± 0.001	11.52 ± 0.014
Zn II	[14.36]	12.18 ± 0.002	[14.36]

Table C.5: Column densities for χ Oph in logarithmic scale, determined using the Voigt-profile fitting software `fits6p`.

Ion	Total	Group 1 Comps 1 – 4 [–34.97, –22.39] km/s	Group 2 Comps 5 – 9 [–20.8, –15.33] km/s	Group 3 Comps 10 – 15 [–12.73, –6.43] km/s	Group 4 Comps 16 – 17 [–4.49, 0.65] km/s
H _{tot}	21.31 ± 0.10				
H I	21.21 ± 0.03				
H ₂	20.63 ± 0.1				
Cr II	13.02 ± 0.094	12.48 ± 0.066	12.13 ± 0.033	12.77 ± 0.047	11.51 ± 0.046
Fe II	14.88 ± 0.07	14.16 ± 0.045	13.88 ± 0.023	14.71 ± 0.042	13.34 ± 0.032
Ge II	12.37 ± 0.001	10.89 ± 0.02	11.55 ± 0.019	12.26 ± 0.039	10.94 ± 0.014
Mg II	15.71 ± 0.045	14.91 ± 0.016	15.11 ± 0.016	15.46 ± 0.039	14.25 ± 0.011
Mn II	13.28 ± 0.015	12.26 ± 0.009	12.51 ± 0.005	13.13 ± 0.011	11.53 ± 0.006
Ni II	13.45 ± 0.023	12.97 ± 0.016	12.54 ± 0.012	13.14 ± 0.01	12.16 ± 0.01
O I	17.92 ± 0.105	16.69 ± 0.069	17.06 ± 0.057	17.83 ± 0.046	< 16.68
P II	14.41 ± 0.231	13.37 ± 0.074	13.71 ± 0.073	14.25 ± 0.198	12.73 ± 0.049
Ti II	11.54 ± 0.028	11.4 ± 0.025	10.6 ± 0.011	10.65 ± 0.009	9.62 ± 0.008
Zn II	13.60 ± 0.07	12.38 ± 0.02	12.81 ± 0.01	13.48 ± 0.09	11.67 ± 0.08

Table C.6: Column densities for HD 154368 in logarithmic scale, determined using the Voigt-profile fitting software `VoigtFit`.

Ion	Total	Group 1 Comps 1 – 2 [–27.7, –20.7] km/s	Group 2 Comps 3 –15 km/s	Group 3 Comps 4 – 5 [–11.3, –9.3] km/s	Group 4 Comps 6 – 8 [–6.5, 0.1] km/s	Group 5 Comps 9 – 11 [4.2, 13.1] km/s
H _{tot}	21.52 ± 0.11					
H I	21.27 ± 0.05					
H ₂	21.16 ± 0.10					
Ca II	12.71 ± 0.054	11.54 ± 0.024	11.42 ± 0.037	12.24 ± 0.1	12.31 ± 0.202	11.76 ± 0.868
Cr II	13.31 ± 0.036	12.05 ± 0.122	11.76 ± 0.238	12.92 ± 0.004	12.93 ± 0.055	12.18 ± 0.01
Fe II	15.11 ± 0.035	13.85 ± 0.118	13.19 ± 0.512	14.73 ± 0.003	14.74 ± 0.013	13.97 ± 0.086
Mg II	16.2 ± 0.041	15.12 ± 0.077	14.88 ± 0.147	15.51 ± 0.01	15.98 ± 0.013	14.86 ± 0.078
Mn II	13.49 ± 0.095	12.51 ± 0.186	12.25 ± 0.326	–	13.33 ± 0.047	12.41 ± 0.073
Ni II	13.76 ± 0.039	12.34 ± 0.189	12.27 ± 0.229	13.34 ± 0.005	13.36 ± 0.006	12.75 ± 0.179
O I	17.98 ± 0.034	15.7 ± 1.069	–	16.34 ± 0.001	17.97 ± 0.043	–
P II	14.44 ± 0.03	13.26 ± 0.079	12.7 ± 0.187	13.73 ± 0.009	14.3 ± 0.005	11.4 ± 1.177
Ti II	12.01 ± 0.021	10.69 ± 0.048	10.45 ± 0.1	11.64 ± 0.002	11.41 ± 0.013	11.33 ± 0.123
Zn II	[13.57]	12.64 ± 0.039	12.73 ± 0.191	[12.8]	[13.28]	[12.17]

Table C.7: Column densities for κ Aql in logarithmic scale, determined using the Voigt-profile fitting software `fits6p`.

Ion	Total	Group 1 Comps 1 – 3 [–28.2, –18.2] km/s	Group 2 Comps 4 – 6 [–16.2, –11.1] km/s	Group 3 Comps 7 – 8 [–8.7, –6.2] km/s	Group 4 Comps 9 – 10 [–2.1, 1.5] km/s	Group 5 Comps 11 – 13 [5.8, 13.9] km/s
H _{tot}	21.03 ± 0.10					
H I	20.94 ± 0.03					
H ₂	20.31 ± 0.10					
Cr II	12.99 ± 0.02	11.97 ± 0.08	12.68 ± 0.03	12.26 ± 0.05	11.62 ± 0.12	12.25 ± 0.04
Fe II	14.74 ± 0.01	13.7 ± 0.05	14.42 ± 0.02	14.03 ± 0.03	13.38 ± 0.08	14.02 ± 0.03
Mg II	15.66 ± 0.01	14.46 ± 0.05	15.52 ± 0.02	14.89 ± 0.03	13.81 ± 0.18	14.23 ± 0.09
Mn II	13.17 ± 0.04	12.01 ± 0.14	13.02 ± 0.05	12.48 ± 0.07	< 10.82	11.53 ± 0.74
Ni II	13.41 ± 0.02	12.59 ± 0.04	12.95 ± 0.03	12.61 ± 0.04	12.15 ± 0.08	12.85 ± 0.02
O I	17.85 ± 0.03	16.79 ± 0.13	17.66 ± 0.03	17.04 ± 0.07	16.64 ± 0.14	16.47 ± 0.33
P II	14.32 ± 0.01	12.92 ± 0.07	14.2 ± 0.02	13.54 ± 0.02	< 12.43	12.71 ± 0.12
Ti II	11.64 ± 0.02	11.0 ± 0.02	11.16 ± 0.03	10.79 ± 0.06	10.46 ± 0.06	11.0 ± 0.04
Zn II	13.33 ± 0.04	11.91 ± 0.02	13.15 ± 0.05	12.75 ± 0.02	11.16 ± 0.10	11.76 ± 0.03

Table C.8: Column densities for HD 206267 in logarithmic scale, determined using the Voigt-profile fitting software VoigtFit.

Ion	Total	Group 1 Comps 1 – 2 [–32.1, –36.7] km/s	Group 2 Comps 3 – 7 [–14.6, –5.3] km/s
H _{tot}	21.39 ± 0.11		
H I	21.24 ± 0.04		
H ₂	20.86 ± 0.10		
Ca II	12.76 ± 0.004	11.84 ± 0.0	12.7 ± 0.001
Cr II	13.3 ± 0.015	11.91 ± 0.011	13.28 ± 0.237
Fe II	15.07 ± 0.008	13.56 ± 0.026	15.05 ± 1.303
Mg II	16.01 ± 0.023	14.48 ± 0.022	15.99 ± 0.416
Mn II	13.55 ± 0.086	12.05 ± 0.077	13.5 ± 0.748
Ni II	13.8 ± 0.041	12.73 ± 0.053	13.75 ± 2.557
O I	18.18 ± 0.06	16.53 ± 0.006	18.17 ± 9.241
P II	14.49 ± 0.016	13.23 ± 0.057	14.46 ± 0.0
Ti II	12.13 ± 0.033	10.61 ± 0.039	12.11 ± 0.043

Table C.9: Column densities for HD 207198 in logarithmic scale, determined using the Voigt-profile fitting software VoigtFit.

Ion	Total	Group 1 Comps 1 – 2 [–34.3, –27.8] km/s	Group 2 Comps 3 – 6 [–22.1, –9.8] km/s	Group 3 Comps 7 4.7 km/s
H _{tot}	21.41 ± 0.11			
H I	21.28 ± 0.04			
H ₂	20.83 ± 0.10			
Cr II	13.39 ± 0.008	12.89 ± 0.002	13.22 ± 0.001	–
Fe II	15.14 ± 0.009	14.47 ± 0.003	15.02 ± 0.001	13.43 ± 0.091
Mg II	16.08 ± 0.026	15.6 ± 0.012	15.9 ± 0.013	14.32 ± 0.237
Mn II	13.43 ± 0.053	12.81 ± 0.009	13.3 ± 0.04	–
Ni II	13.84 ± 0.025	13.24 ± 0.018	13.69 ± 0.008	12.2 ± 0.184
O I	18.25 ± 0.034	17.74 ± 0.041	18.08 ± 0.017	–
P II	14.64 ± 0.028	14.21 ± 0.01	14.41 ± 0.026	13.33 ± 0.089
Ti II	12.17 ± 0.026	10.79 ± 0.297	12.06 ± 0.004	11.35 ± 0.038

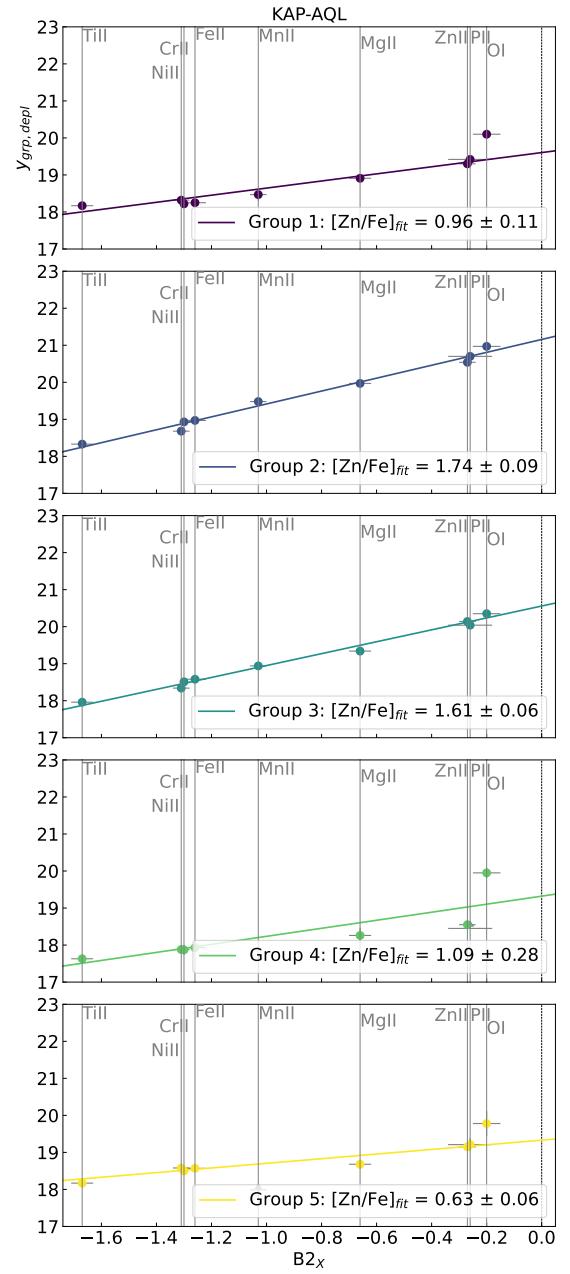
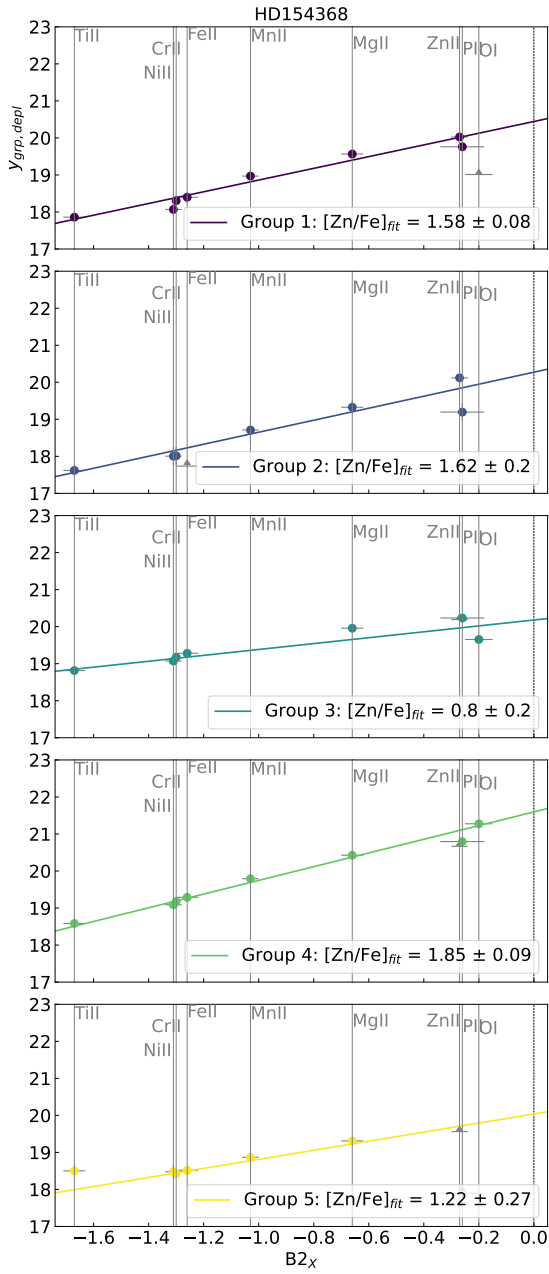


Fig. D.3: Metal patterns for grouped components towards HD 154368.

Fig. D.4: Metal patterns for grouped components towards κ Aql.

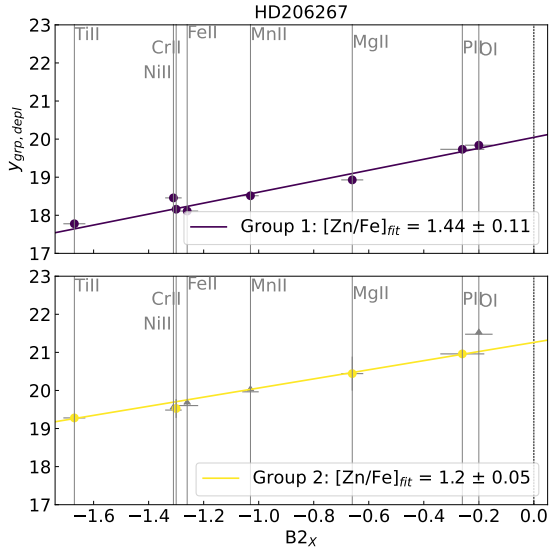


Fig. D.5: Metal patterns for grouped components towards HD 206267.

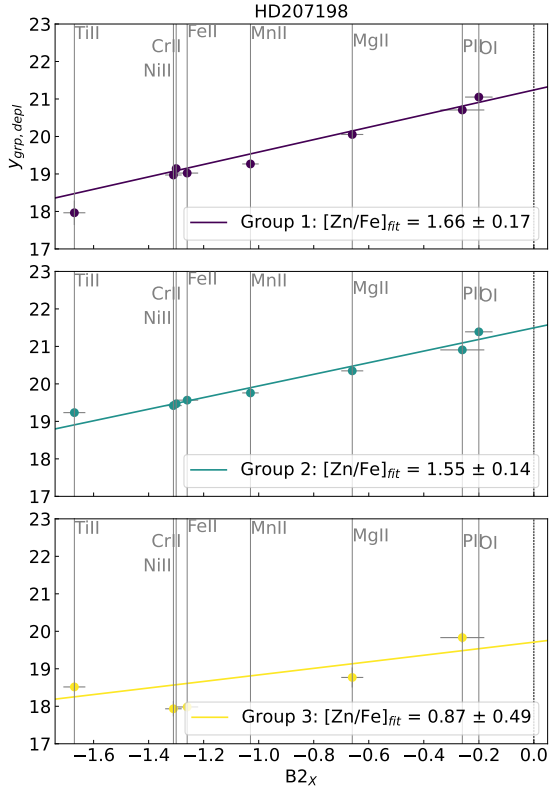


Fig. D.6: Metal patterns for grouped components towards HD 207198.

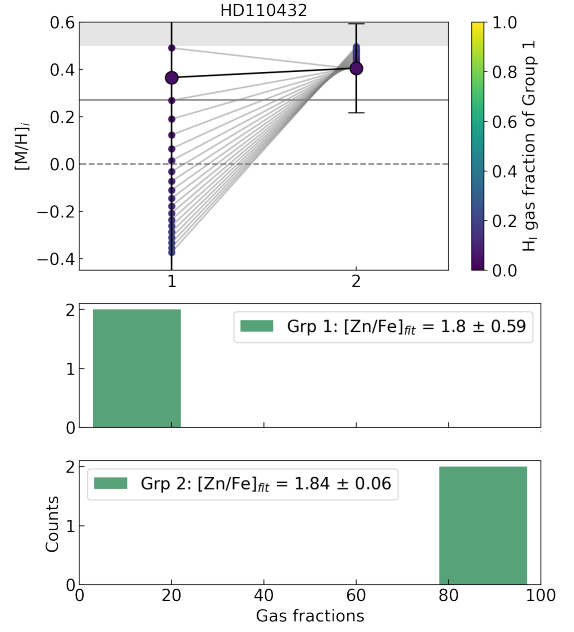


Fig. E.1: The same as Fig. 5, but for HD 110432.

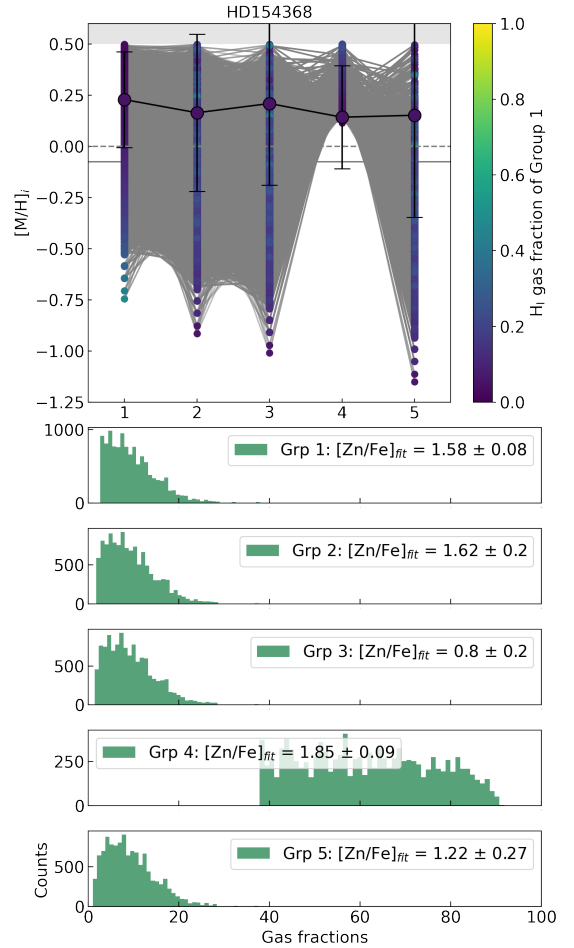


Fig. E.2: The same as Fig. 5, but for HD 154368.

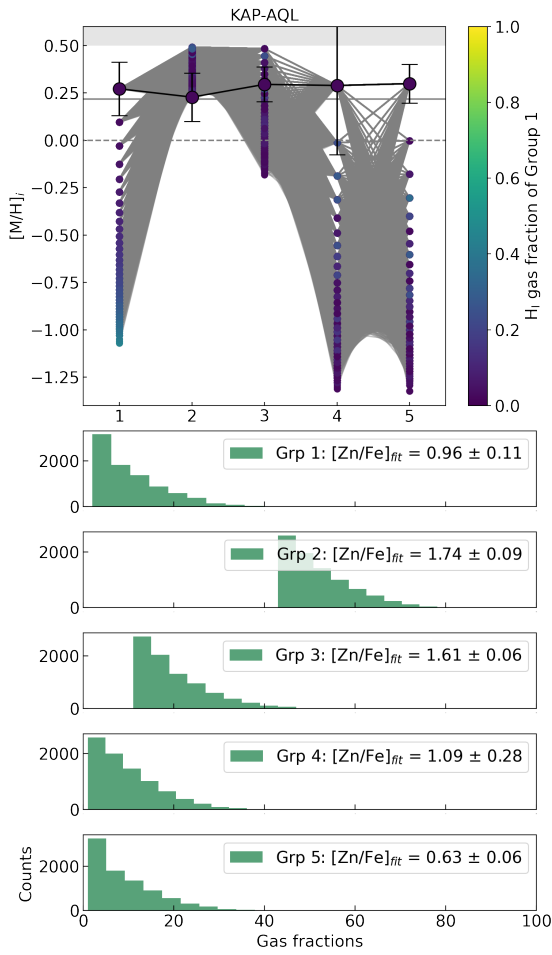


Fig. E.3: The same as Fig. 5, but for κ Aql.

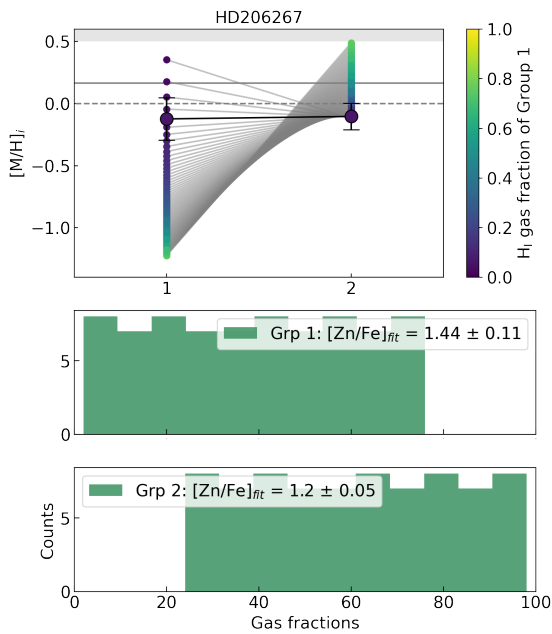


Fig. E.4: The same as Fig. 5, but for HD 206267.

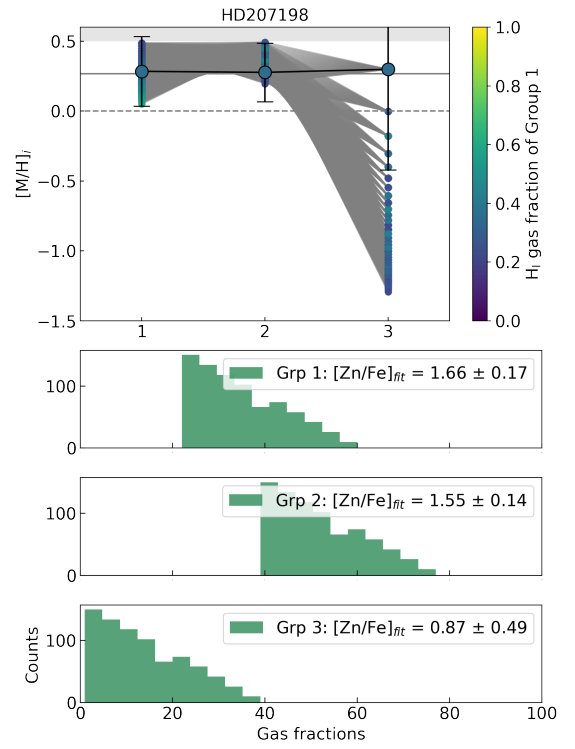


Fig. E.5: The same as Fig. 5, but for HD 207198.

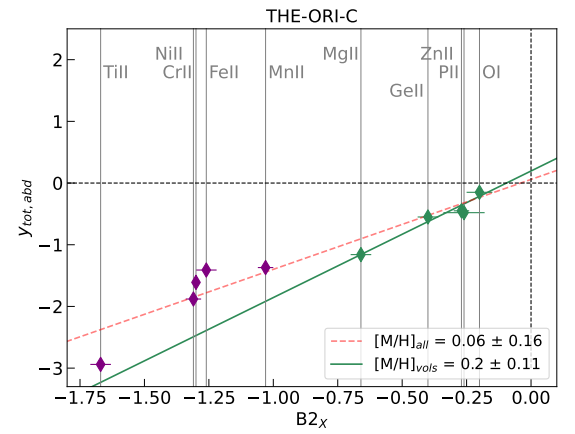


Fig. F.1: Abundance pattern for θ^1 Ori C. The red dashed line shows the fit to all metals. For this line of sight, the fit to the more refractory metals gives a high metallicity of 1.77 ± 0.96 , which is not physical. We therefore exclude this, and only show the fit to all metals and the more volatile metals.

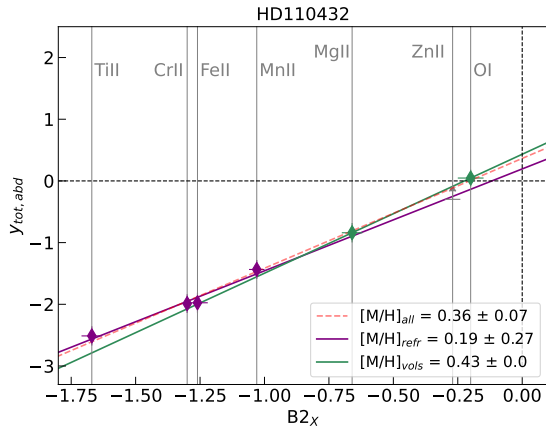


Fig. F.2: Abundance pattern for HD 110432. The red dashed line shows the fit to all of the metals, the purple is the fit to the more refractory metals, and the green is fit to the more volatile. The grey dashed horizontal line shows the y -intercept for the fit to all metals.

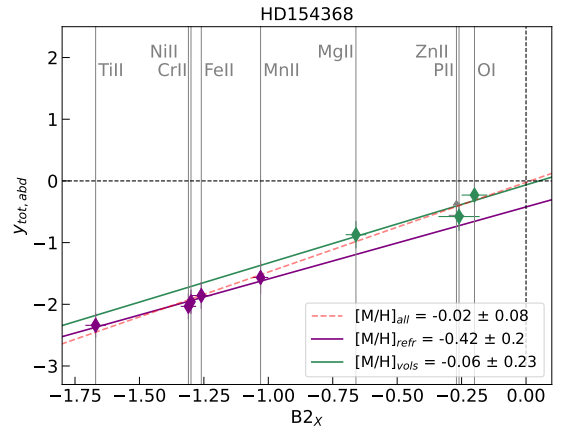


Fig. F.5: Abundance pattern for HD 154368.

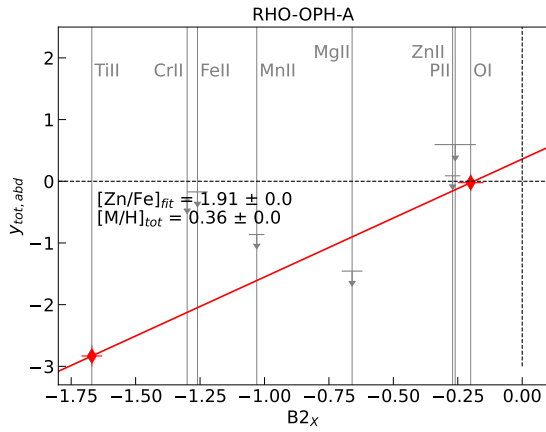


Fig. F.3: Abundance pattern for ρ Oph A. We do not include the column densities for most of the metals because most absorption lines along this line of sight are saturated. The only two reliable metals are Ti II and O I.

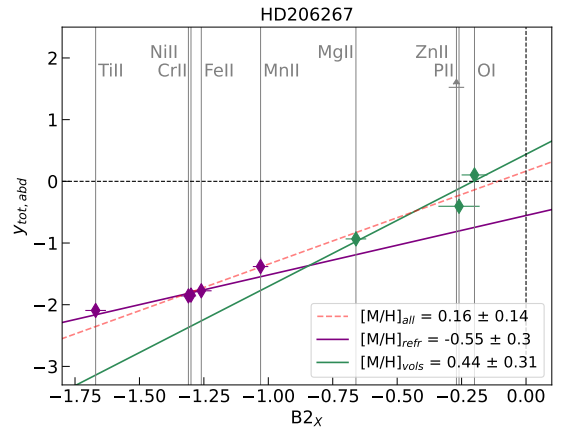


Fig. F.6: Abundance pattern for HD 206267.

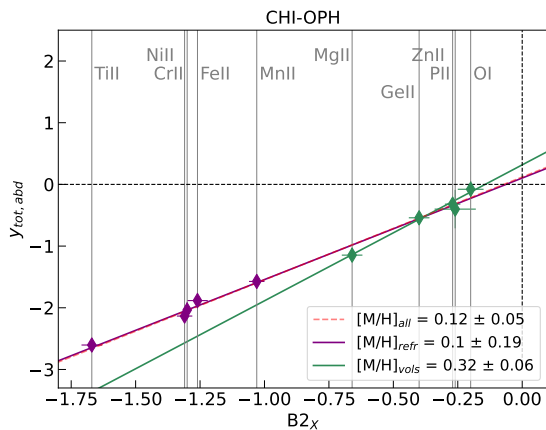


Fig. F.4: Abundance pattern for χ Oph.

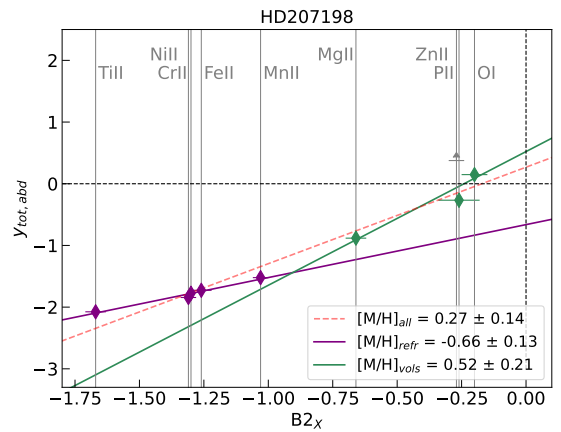
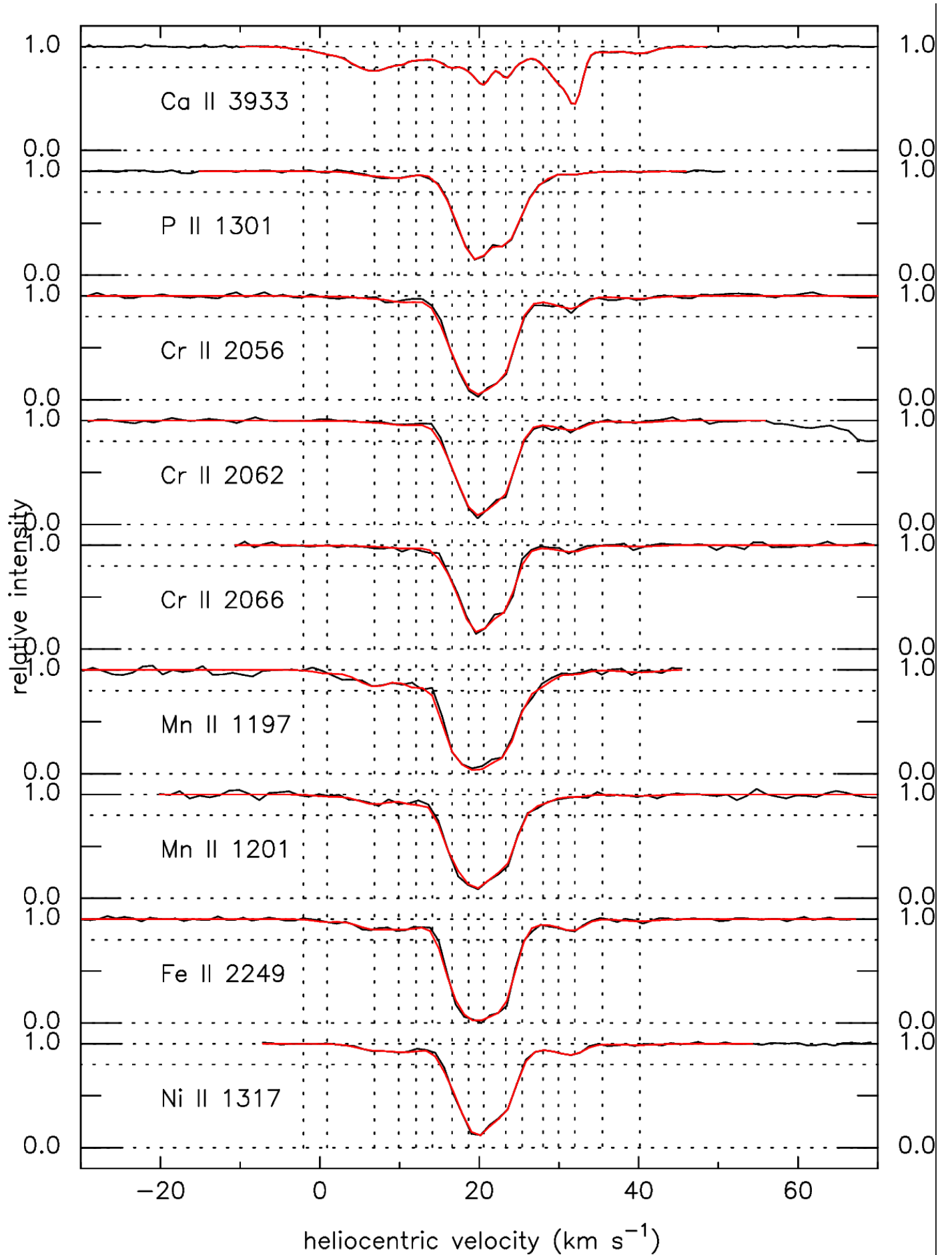


Fig. F.7: Abundance pattern for HD 207198.



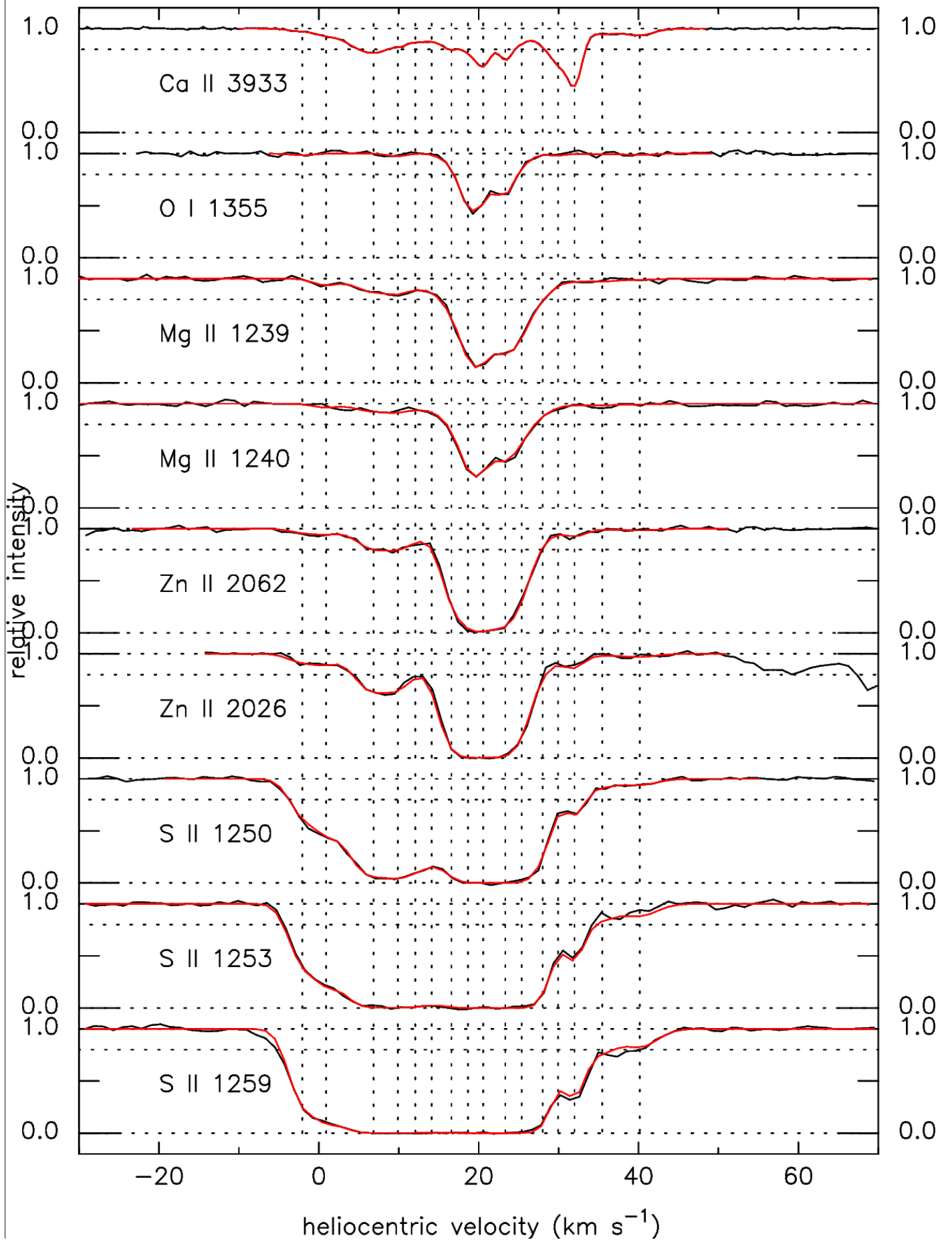


Fig. G.1: continued for θ^1 Ori C.

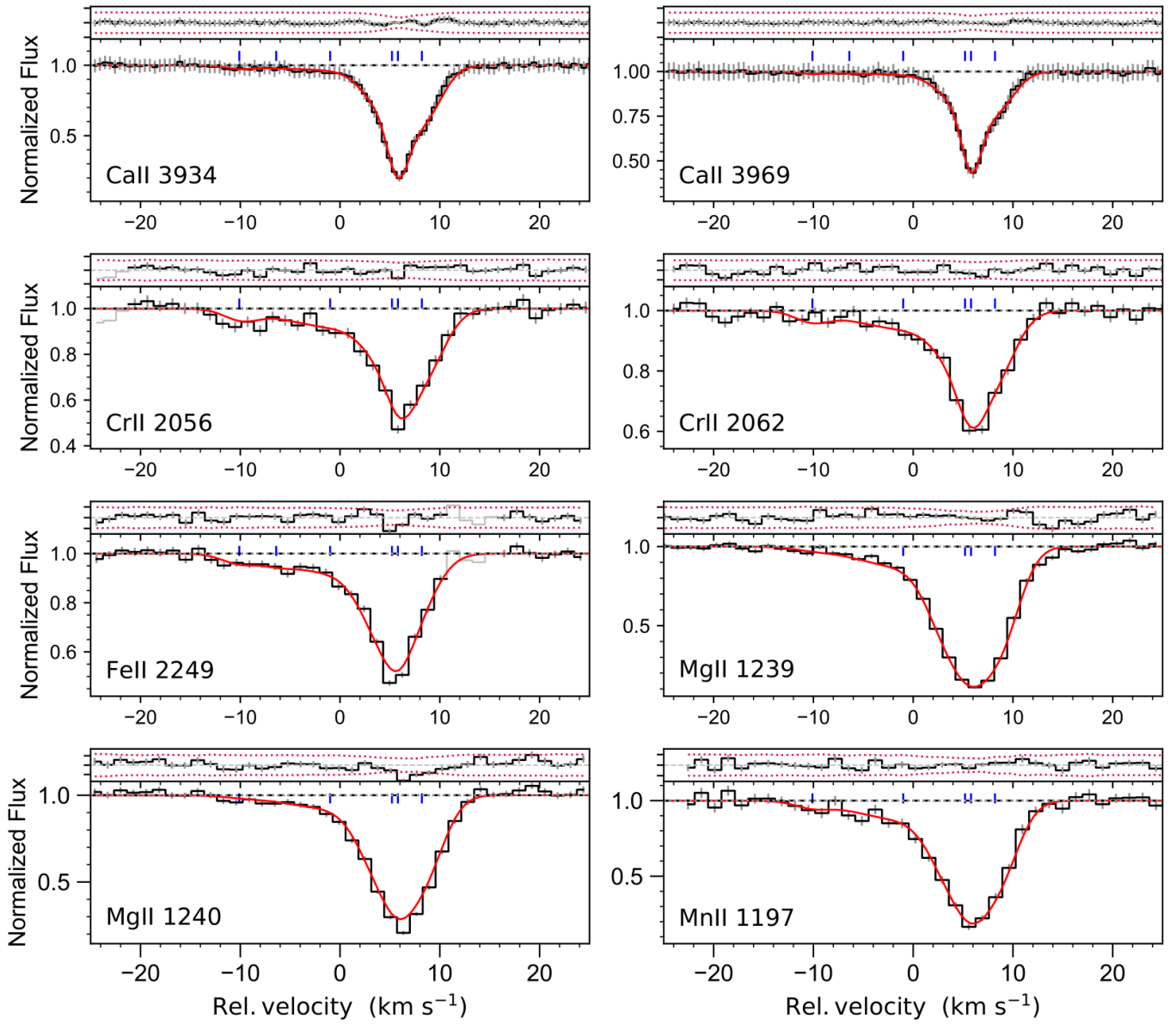


Fig. G.2: Fits to the spectra for HD 110432 using VoigtFit.

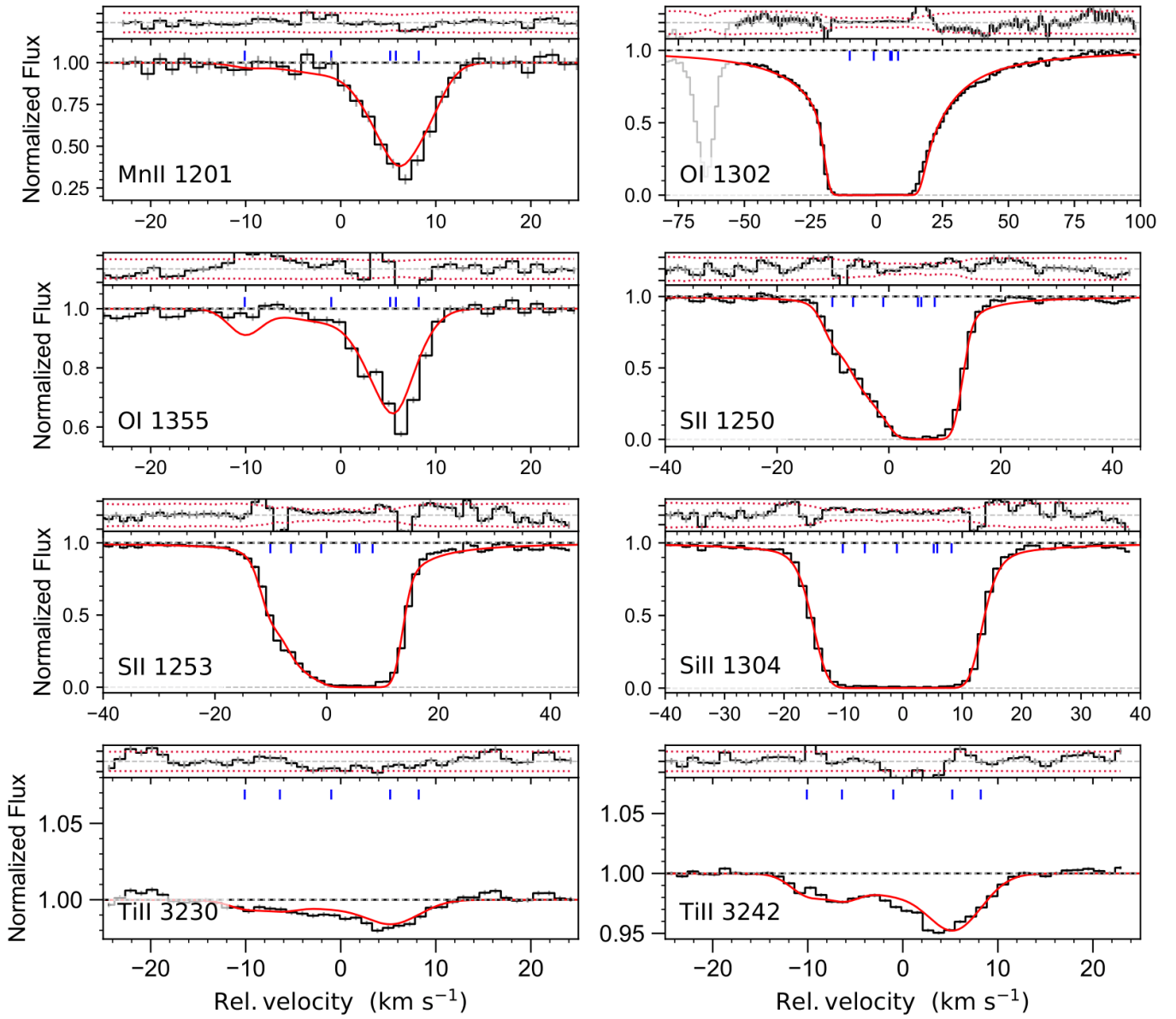


Fig. G.2: continued for HD 110432.

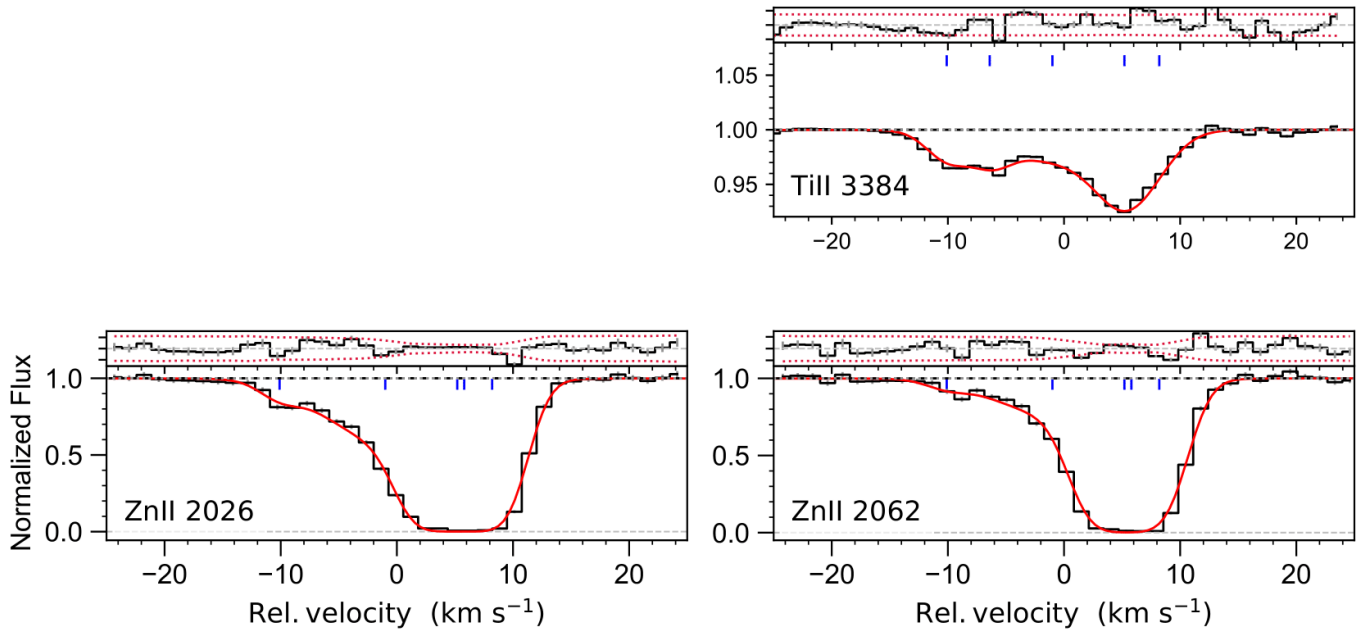


Fig. G.2: continued for HD 110432.

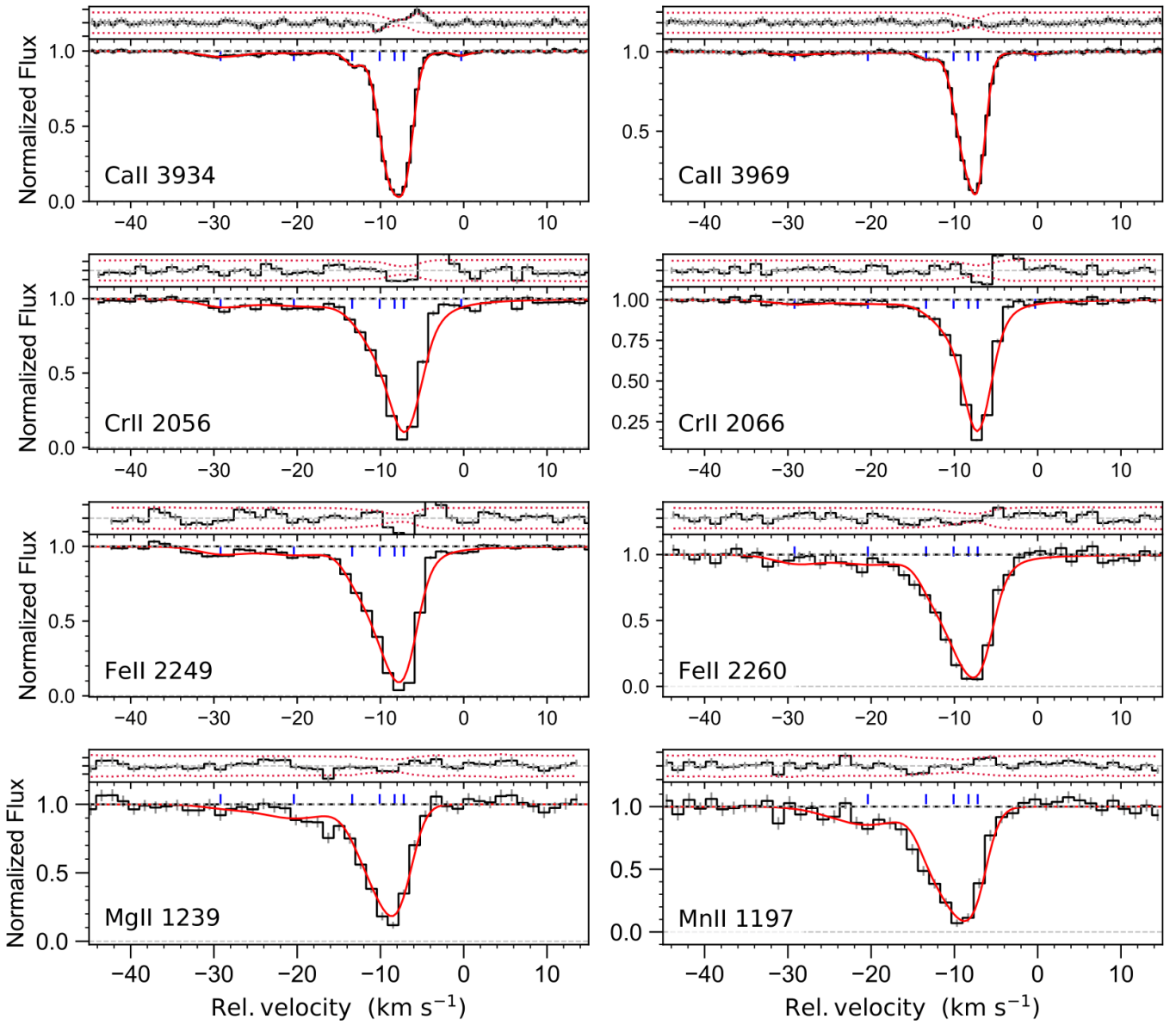


Fig. G.3: Fits to the spectra for ρ Oph A using VoigtFit.

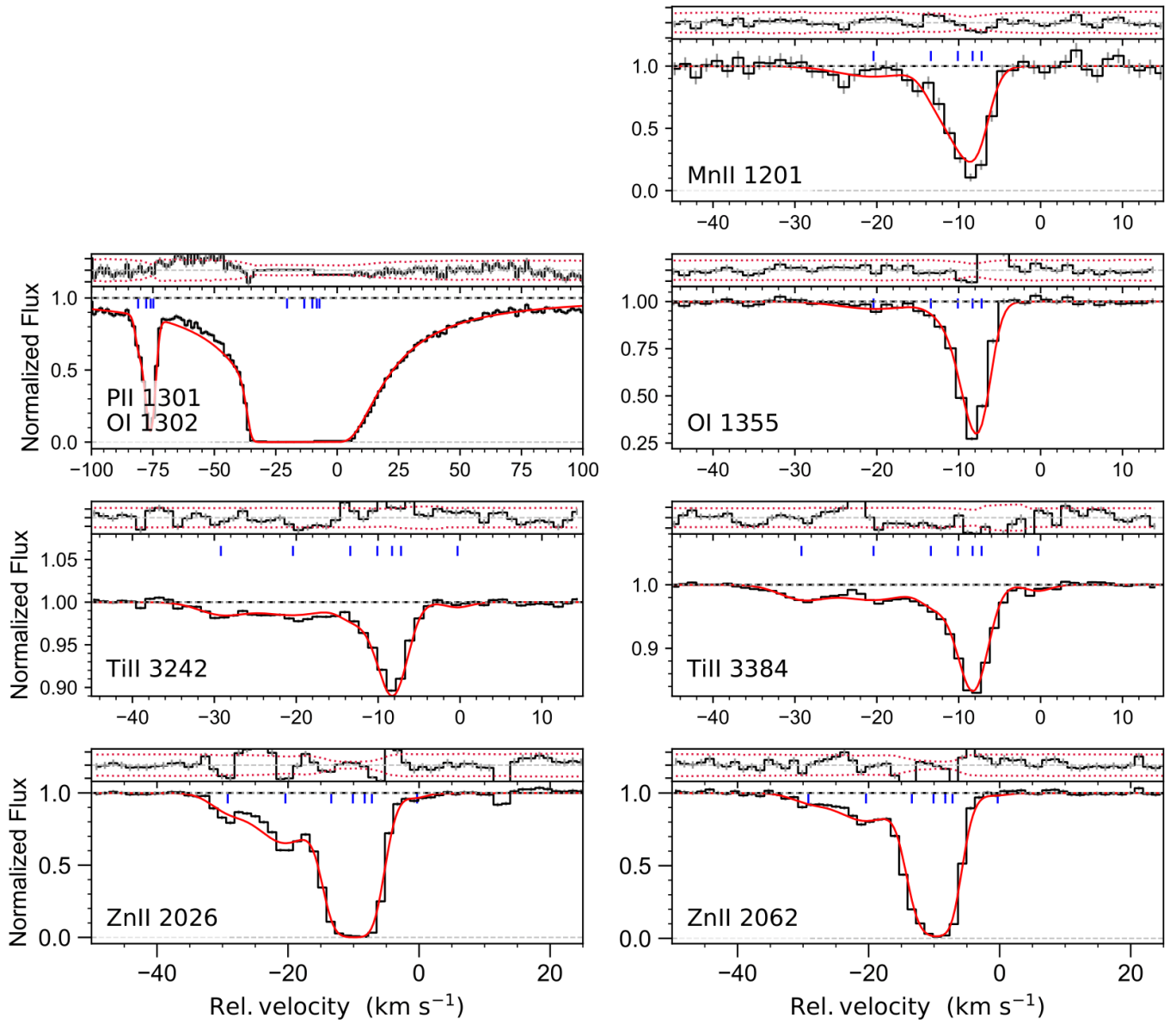


Fig. G.3: continued for ρ Oph A.

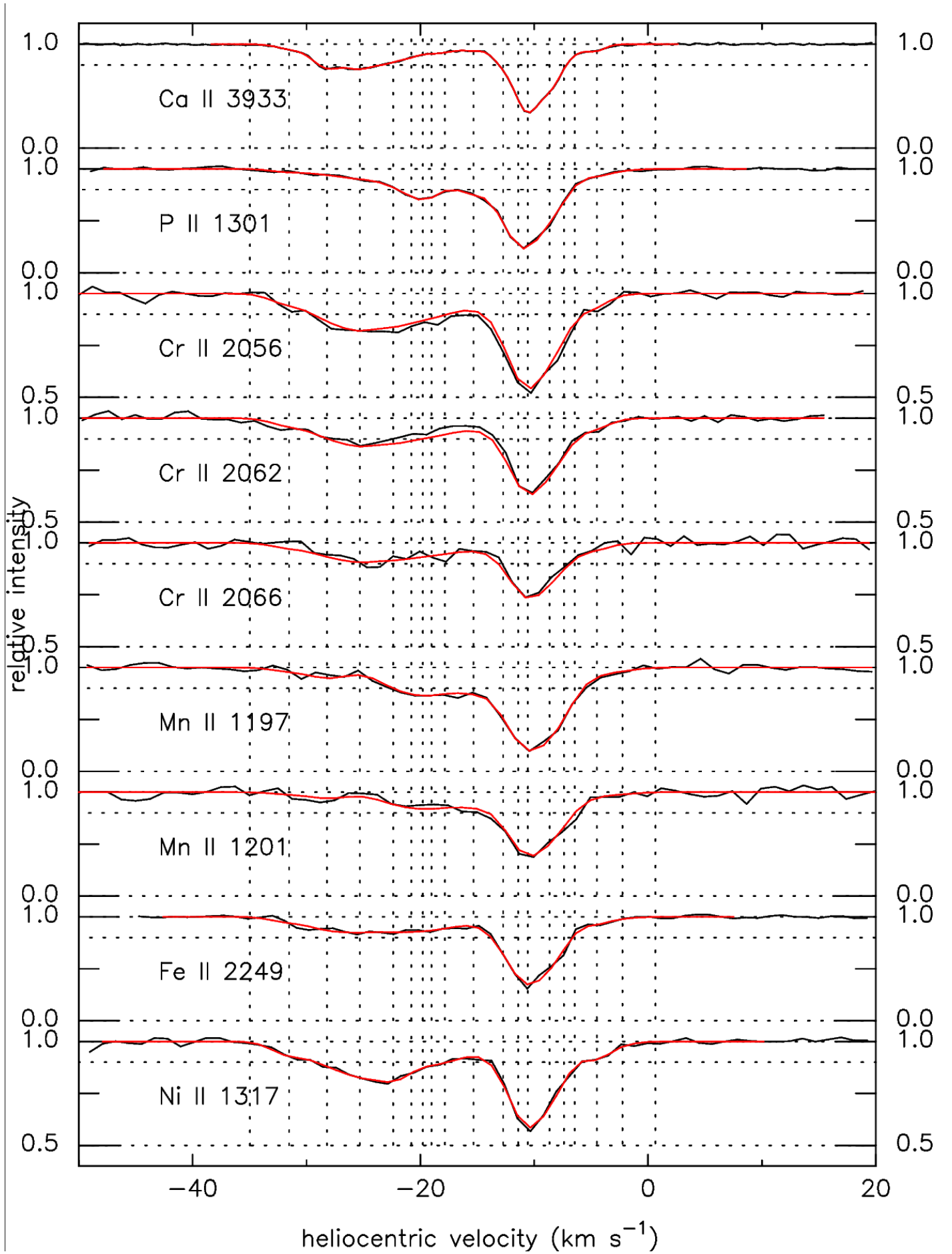
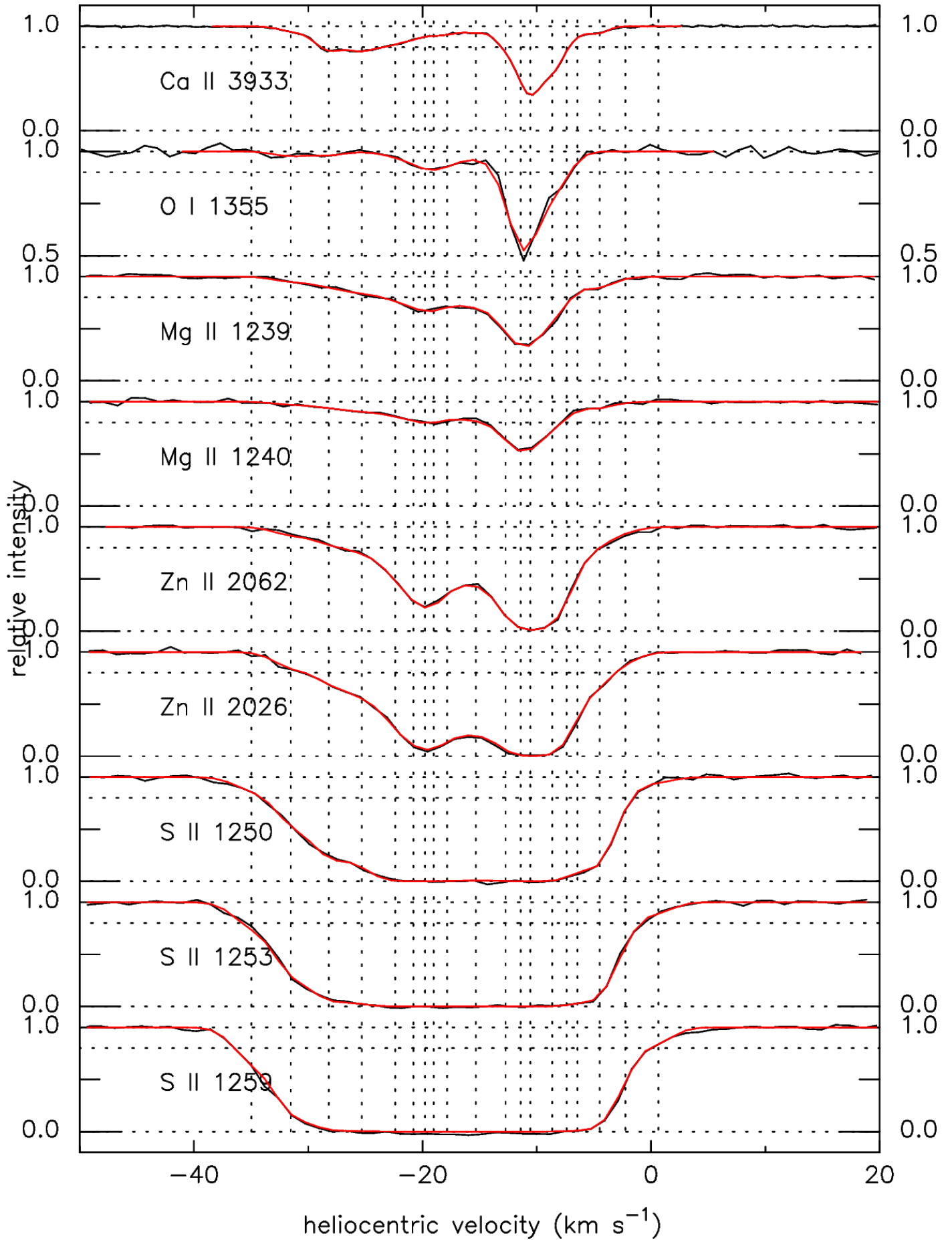


Fig. G.4: Fits to the spectra for χ Oph using fits6p.



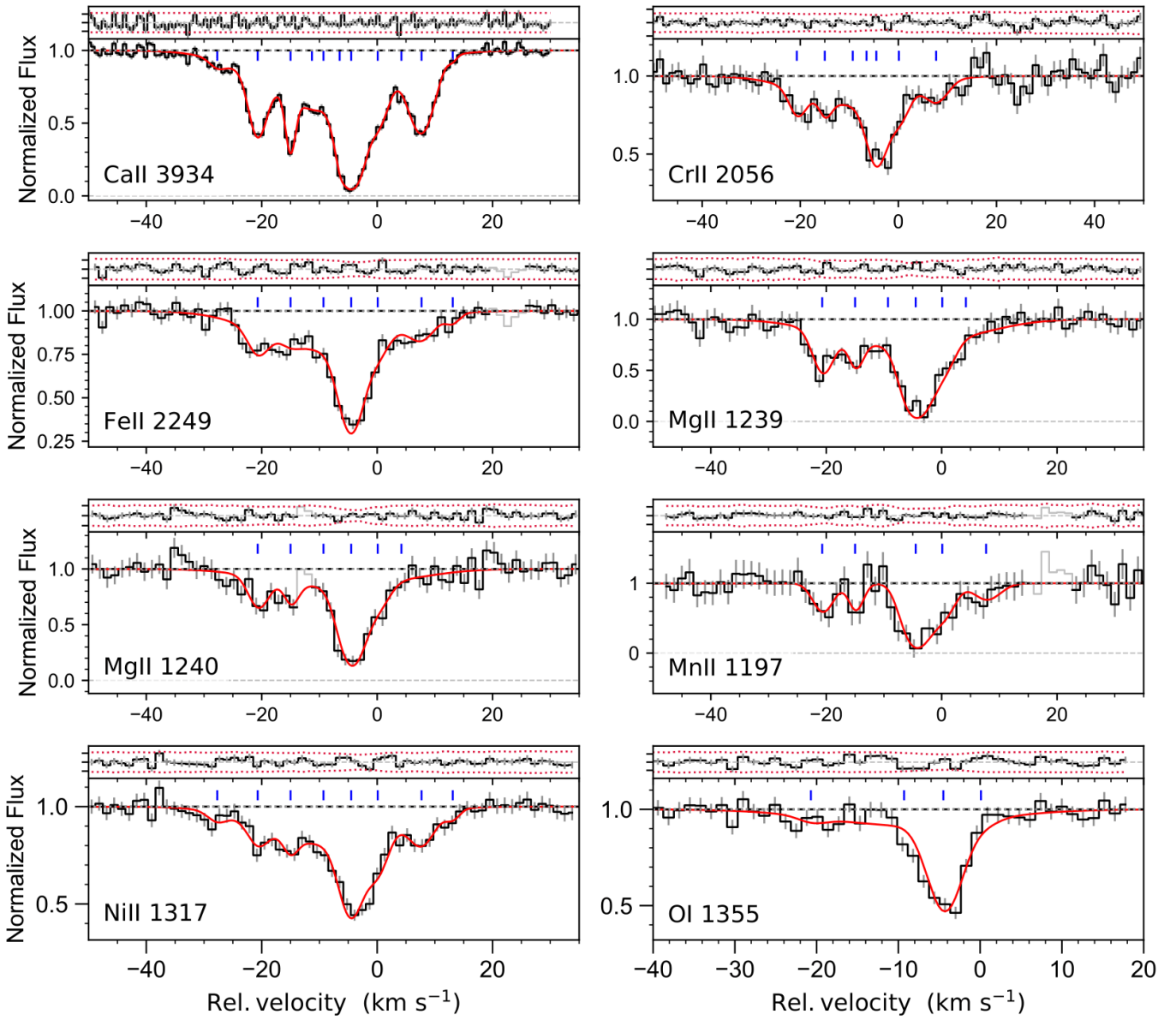


Fig. G.5: Fits to the spectra for HD 154368 using VoigtFit.

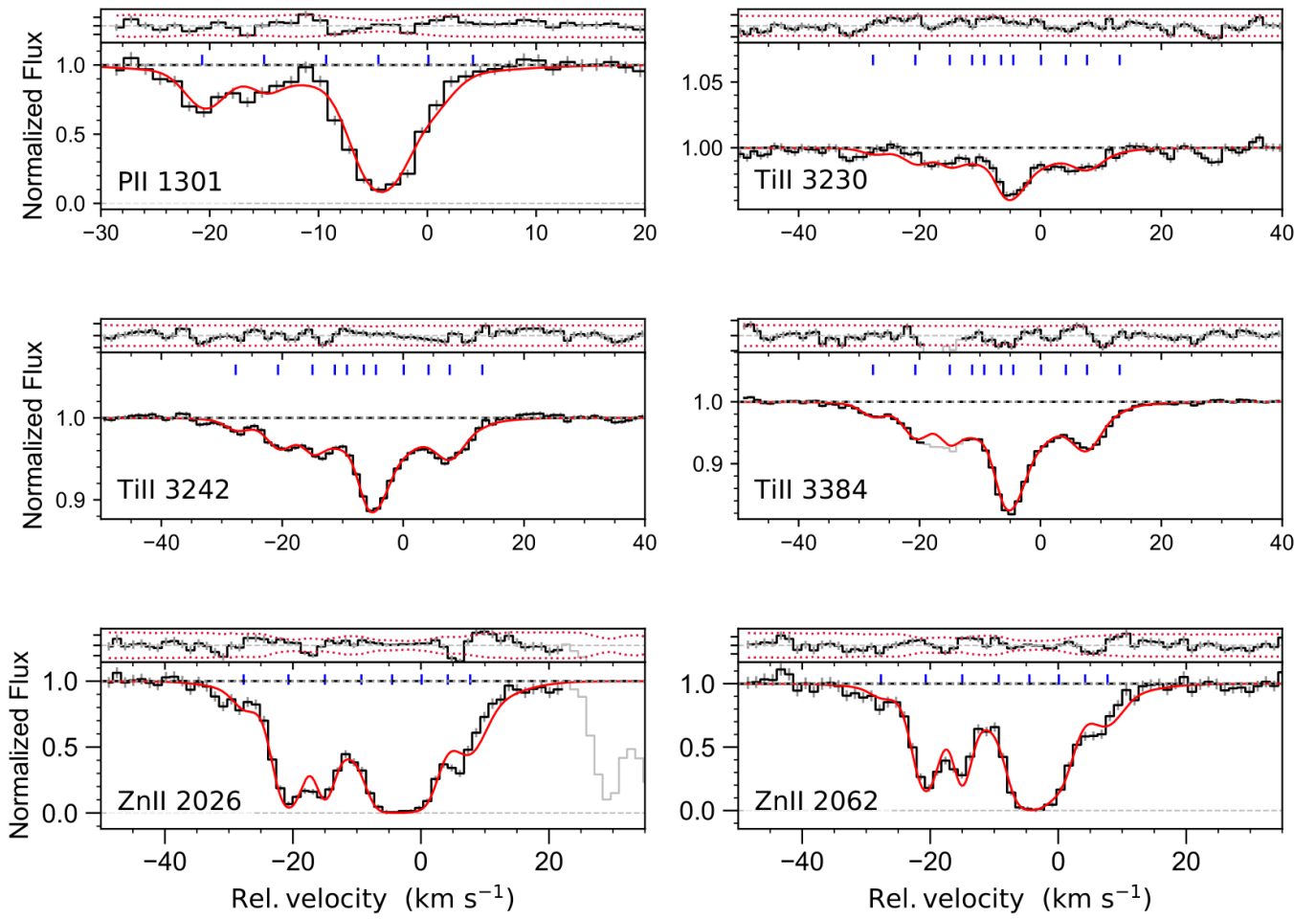


Fig. G.5: continued for HD 154368.

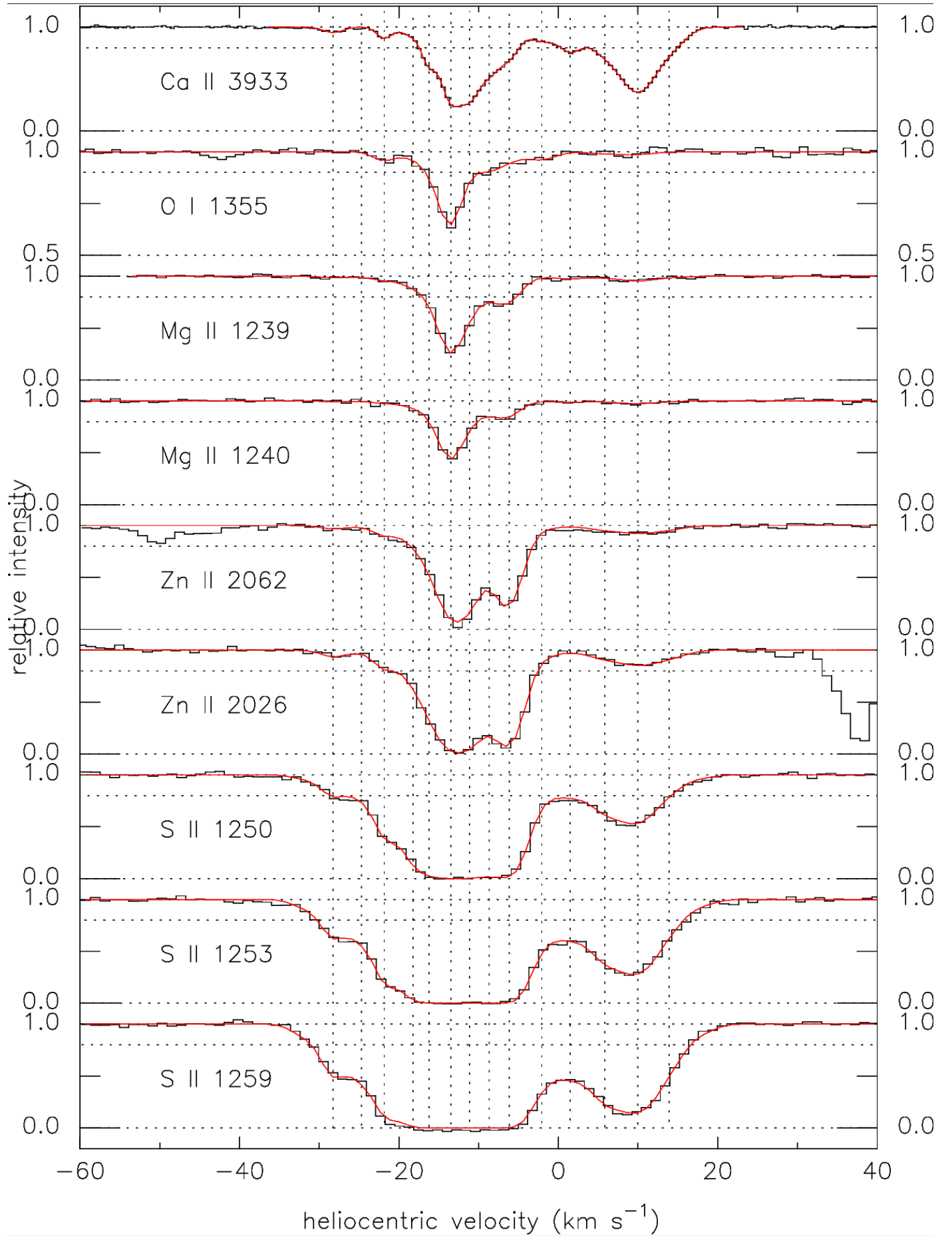
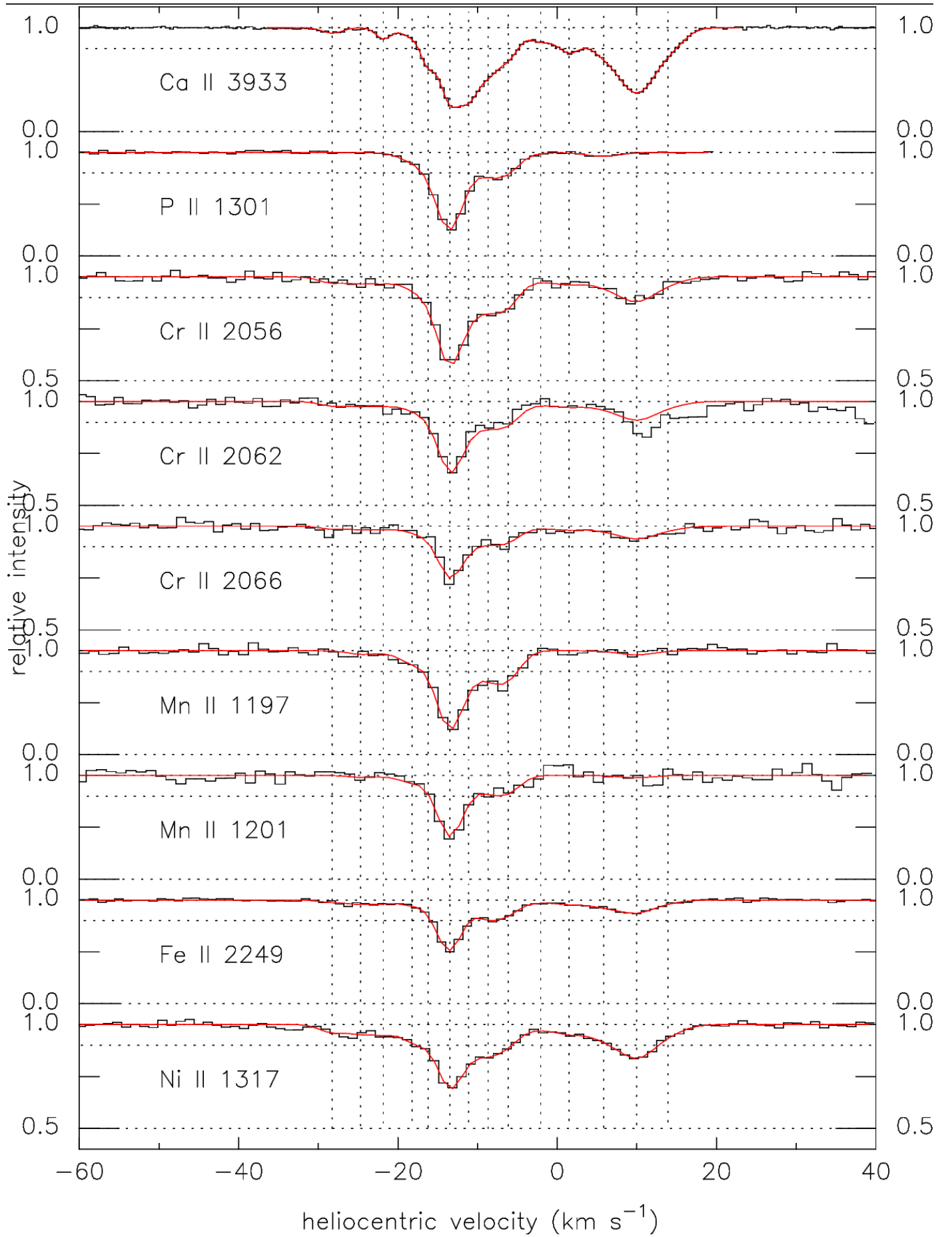


Fig. G.6: Fits to the spectra for κ Aql using `fits6p`.

Fig. G.6: continued for κ Aql.

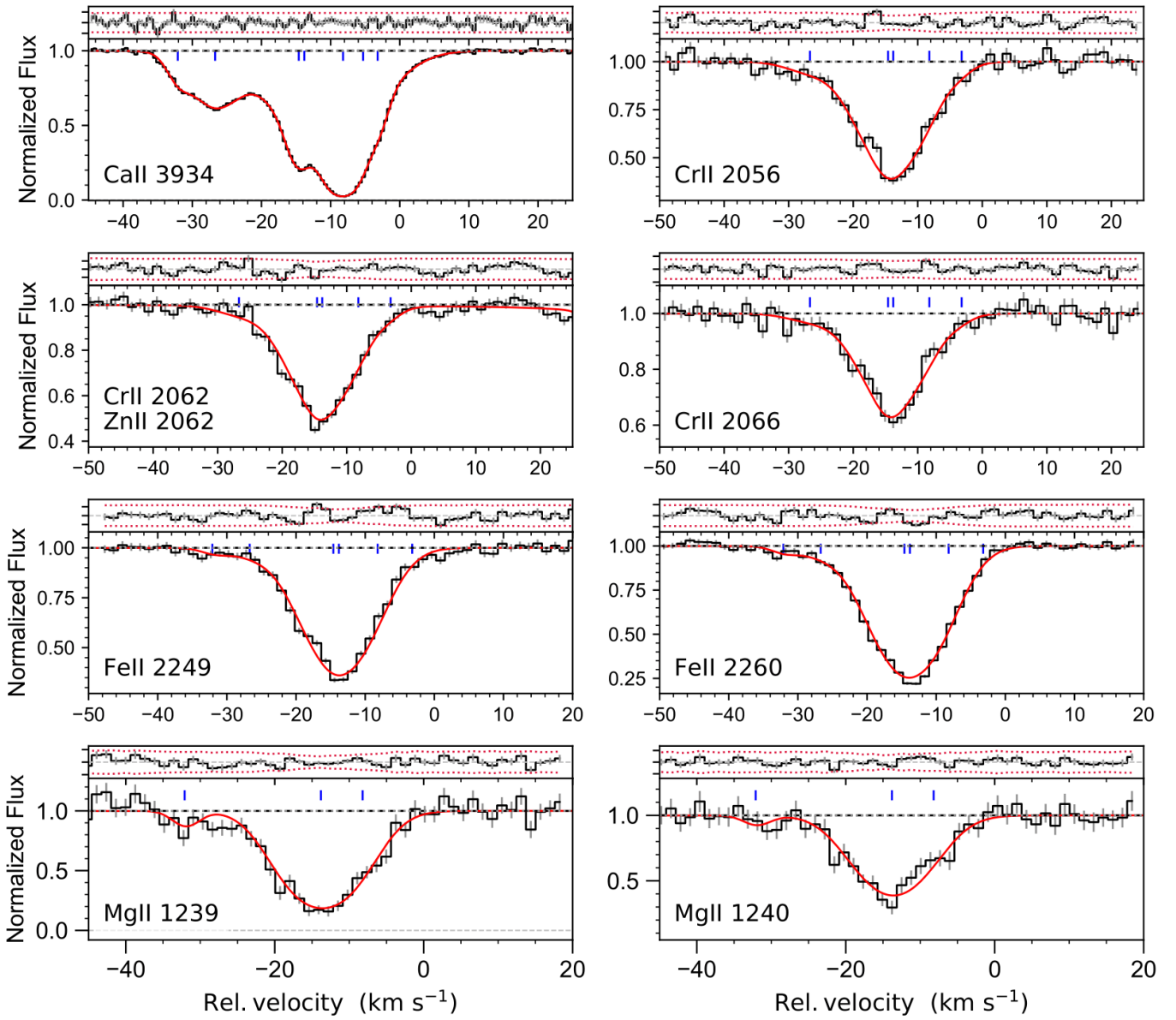


Fig. G.7: Fits to the spectra for HD 206267 using VoigtFit.

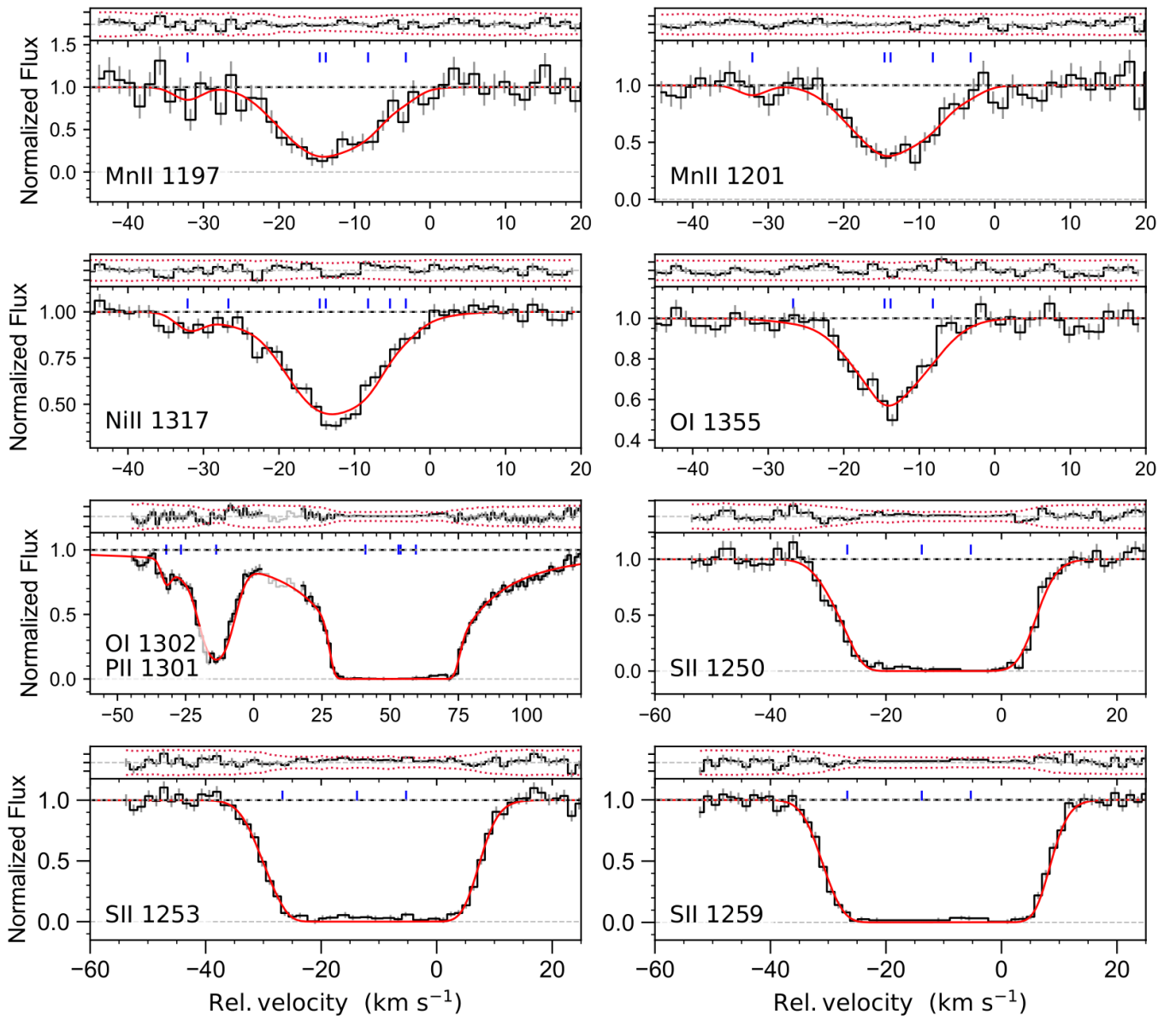


Fig. G.7: continued for HD 206267.

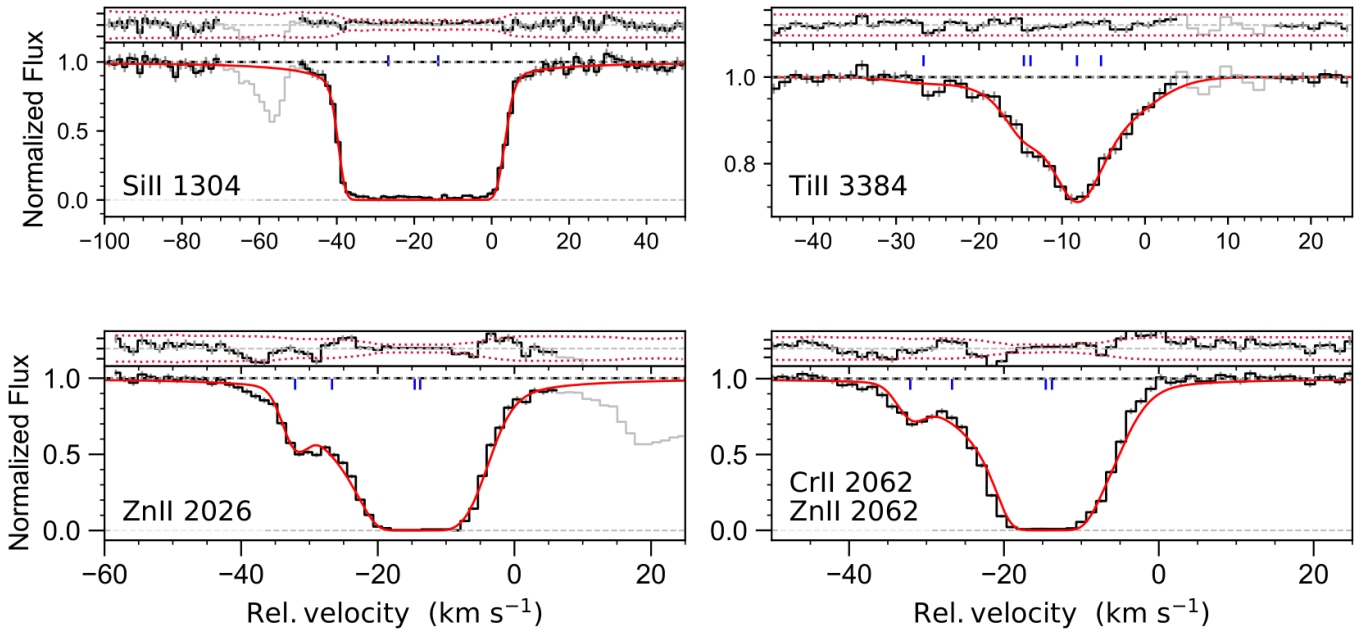


Fig. G.7: continued for HD 206267.

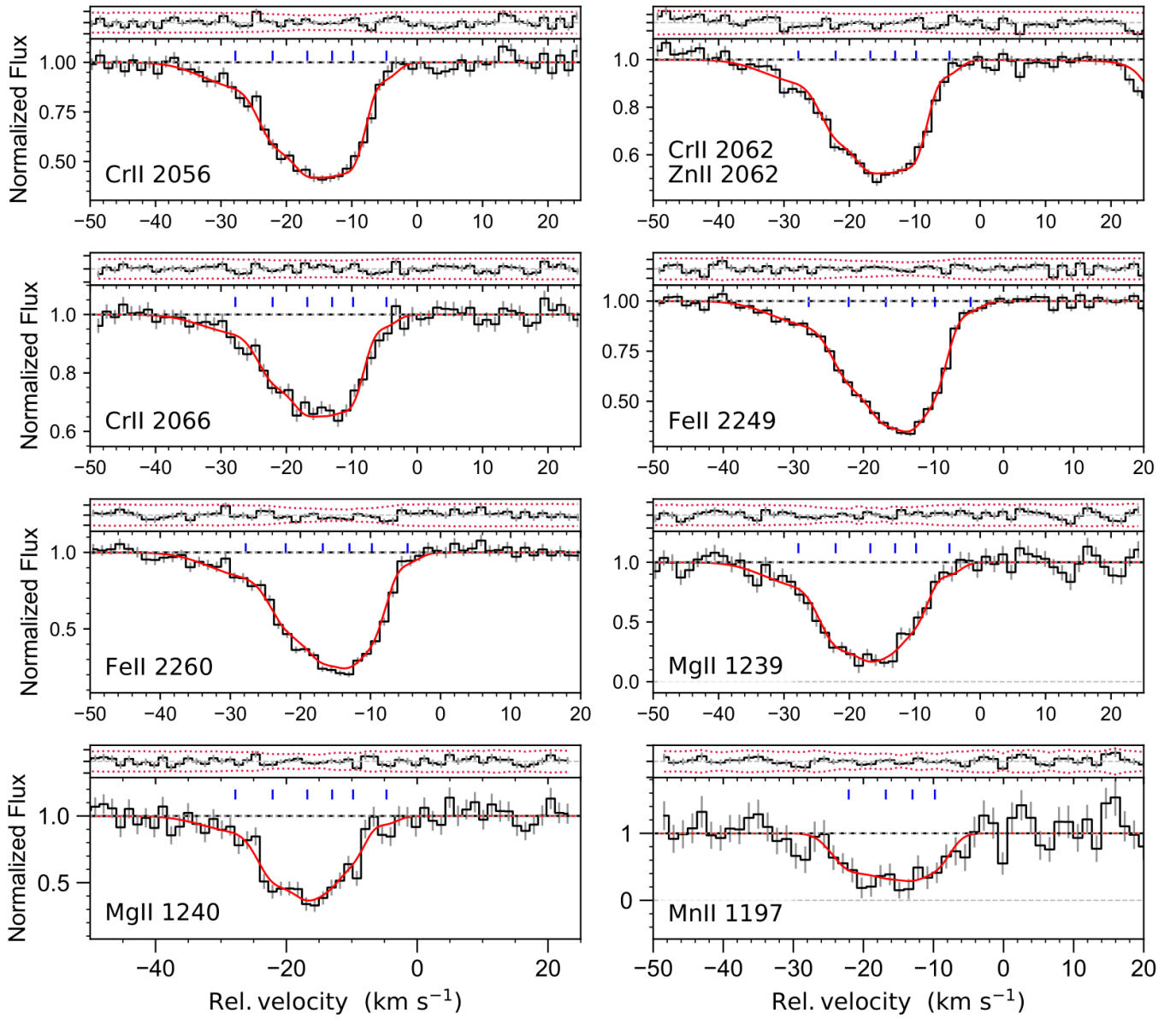


Fig. G.8: Fits to the spectra for HD 207198 using VoigtFit.

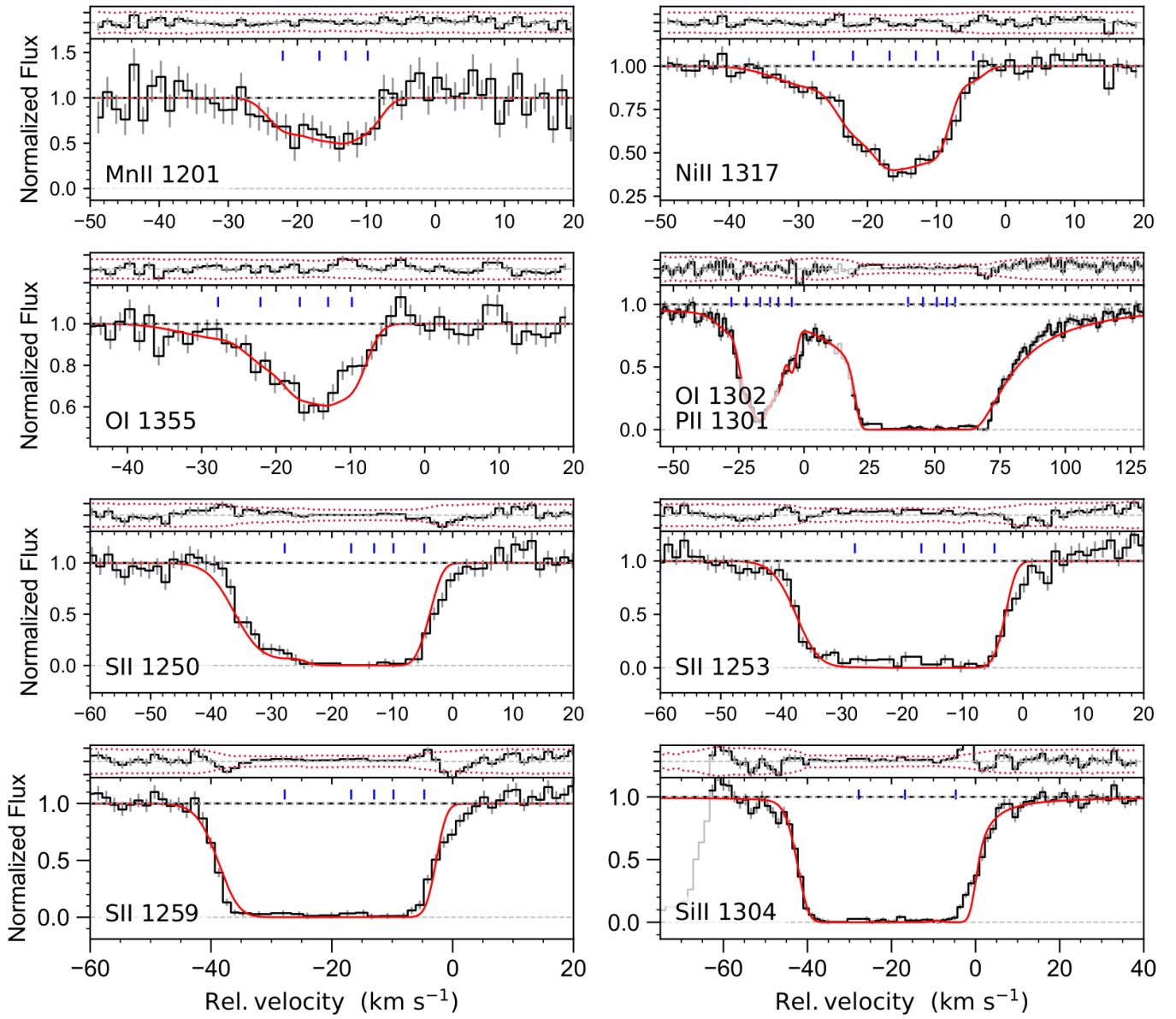


Fig. G.8: continued for HD 207198.

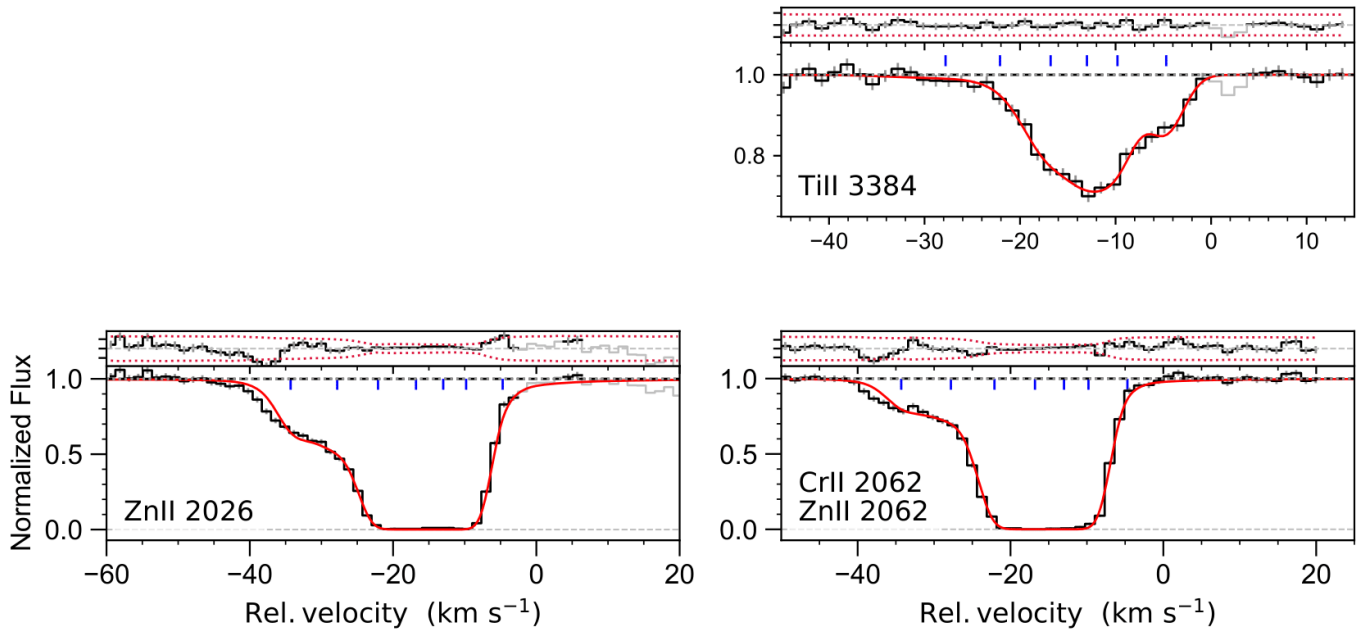


Fig. G.8: continued for HD 207198.